



Characterisation of a 3D-printed alkali-activated material based on waste mineral wool at room and elevated temperatures

Majda Pavlin^{a,*}, Barbara Horvat^a, Romana Cerc Korošec^b, Rok Capuder^c, Lidija Korat^a, Vilma Ducman^a

^a Slovenian National Building and Civil Engineering Institute, Dimičeva Ulica 12, 1000, Ljubljana, Slovenia

^b Faculty of Chemistry and Chemical Technology, Večna Pot 113, 1000, Ljubljana, Slovenia

^c Zavod 404, Mencingerjeva Ulica 7, 1000, Ljubljana, Slovenia

ARTICLE INFO

Keywords:

Alkali-activated material
Waste mineral wool
Upcycling
Material extrusion
Porosity
Thermal exposure

1. Introduction

The building sector is the largest energy consumer in the European Union (EU), accounting for approximately 40 % of energy consumption and 36 % of CO₂ emissions [1]. The demand for housing is expected to rise because of the increase in global population. Consequently, construction and demolition waste (CDW), which currently constitutes approximately 25–30 % of the total waste generated annually in Europe [2], will also increase, making it necessary to use it appropriately instead of being dumped in landfills. Additive manufacturing (3D printing) has gained significant attention over the last few years and has served as an encouraging method for solving several environmental problems, including the need for both local source materials and minimising waste production. 3D printing enables the production of more complex shapes and has been employed in various fields [3,4].

Additive manufacturing offers advantages such as freedom of design, reduced labour, customisation, automation, waste minimisation, and the ability to build complex structures with inexpensive materials. However, it also suffers from disadvantages such as the formation of voids between layers, which results in higher porosity and reduced adhesion between printed layers and anisotropic behaviour. These disadvantages represent the challenges in additive manufacturing that need to be overcome [5]. Various types of additive manufacturing methods are currently in use, including binder jetting, directed energy

deposition, material extrusion, material jetting, powder bed fusion, sheet lamination, and vat photo-polymerization [6]. Extrusion and layered printing are most commonly applied for concrete-type materials [7,8].

Printable materials should have suitable workability, extrudability, pumpability, open time, buildability, shape retention, and structural properties, all of which are governed by the properties of the fresh mixture, especially its rheology [6,9–11]. For optimal printability, a balance between various properties must be attained by altering the mix design using a trial-and-error approach [11]. Rheological characteristics are important for extrusion-based printing and are therefore widely studied in the field of cementitious materials [12–15]. The thixotropic behaviour of mixed designs is an influential factor in pumping and printing [16]. The workability of the material is determined using a slump test, where a higher slump height (higher fluidity) corresponds to a lower yield stress [17]. A lower yield stress and viscosity improve pumpability and flow, which are important for extrusion; however, a very low yield stress can cause the shape to collapse after extrusion [5]. The setting time is a useful indicator of the printability window, both of which are important process parameters [10]. Printability refers to the ability of a mixture to extrude (i.e. its extrudability) and maintain its structural integrity when built into layers (i.e. buildability) [18]. For the successful placement of the layers, the setting time of the prepared material should be sufficiently long to enable adequate workability [18,

* Corresponding author. Slovenian National Building and Civil Engineering Institute, Dimičeva Ulica 12, 1000, Ljubljana, Slovenia.

E-mail address: majda.pavlin@zag.si (M. Pavlin).

<https://doi.org/10.1016/j.cemconcomp.2024.105445>

Received 8 September 2022; Received in revised form 8 August 2023; Accepted 15 January 2024

Available online 17 January 2024

0958-9465/© 2024 The Authors. Published by Elsevier Ltd. This is an open access article under the CC BY license (<http://creativecommons.org/licenses/by/4.0/>).

19], flowability, and sufficient adhesiveness between layers [20]. The particle size of the aggregates and/or fibres is limited by the size of the nozzle, and mix designs contain fine powders, inorganic additives (e.g. fly ash-FA), and viscosity modifiers (superplasticisers and accelerators) [14].

A considerable drawback of additive manufacturing on a larger scale is its inability to reinforce materials with fibres, such as polypropylene or PVA, which can increase the tensile strength and ductility but simultaneously change the rheology of the material [21–24]. Further challenges include the spontaneous and in situ nature of adjusting the fresh properties of concrete, formation of cold joints between printed layers, and finishing the final surface of printed concrete objects [25]. The type (material) and size of fibres are both limited in digital fabrication because they can damage the extruder or the pump. Therefore, the pump and nozzle must be designed to enable the printing of specific fibres [26]. Chougan et al. conducted a study in which fibre and nano-clay additives were added to alkali-activated FA, ground granulated blast-furnace slag (GGBFS), and silica fume. A positive impact on the 3D-printed samples was observed with both additives through the incorporation of fibres to fill the voids and a crack-bridging mechanism [27].

Most 3D-printed concrete products use cement-based mix compositions, although other inorganic binders with lower carbon footprints such as alkali-activated materials (AAM) have also been used in recent years [28–32]. AAM is considered a green construction material because its primary constituents such as FA, slag, and glass waste are collected as aluminosilicates from construction/demolition waste [5,6,10,22,26,33–35]. The fresh (and mechanical) properties of AAMs significantly change according to the mix design depending on the type of precursors and activators used, the precursor-activator and water-to-solid (w/s) ratios [36,37]. Thus, there are several possibilities for preparing a suitable mix design for 3D-printed AAMs. Stone wool (SW) and glass wool (GW) are chemically different amorphous fibrous materials that are globally used for thermal and acoustic insulation [38]. Owing to an increase in CDW, there is also a high amount of mineral wool waste, which is problematic for transport and landfilling because of its low density that consumes a considerable amount of space. The EU has set a recycling target for non-hazardous CWD of 70 % by weight [39] to be achieved by 2020 (Waste Framework Directive 2008/98/EC). Although the percentage of utilised mineral wool waste remains low [40], alkali activation currently represents a suitable option for reusing this silicon-rich precursor in the production of new building materials. Mineral wool is composed of fibres (microfibres, owing to the diameter of the fibres) and AAMs contain many unreacted fibres in their gel structure after the activation process [41–43]; therefore, the use of such fibres can increase the structural integrity of the printed objects. The size and arrangement of the particles, as well as the interparticle forces, affect the buildability of the paste [44]. Furthermore, because of the anisotropy, the loading directions affect the 3D-printing process, and reinforcements can improve the bonding between the layers [29]. The chemical compositions of SW and GW differ. GW contains higher amounts of amorphous SiO₂ (59–64 wt%) and Na₂O (approximately 15–18 wt%) compared to that in SW (about 39–43 wt%); higher amounts of Al₂O₃, CaO, and MgO; and less Na₂O [40]. Consequently, different mechanical properties were obtained when SW or GW was used in the alkali activation process. Both types of mineral wools contain organic binders (most commonly phenolic and sugar-based binders) [45]. In our previous study, after 90 days of curing at room temperature, SW reached compressive and bending strengths of 56 MPa and 13 MPa, respectively, and GW reached 80 MPa and 27 MPa, respectively. However, after 3 days of curing at 40 °C, the mechanical properties were found to be higher in the case of GW compared to SW when sodium silicate was used and it was lower when sodium hydroxide was used as the alkali activator [41]. Similarly, Yliniemi et al. observed better mechanical properties of GW when sodium silicate, sodium aluminate, and Na₂CO₃ were added as alkali activators than when NaOH was used [46].

The presence of microfibres improves the bending strength of AAM [47] whereas the presence of organic resin positively affects the compressive strength [42]. In another study, it was found that organic resins influenced the dissolution, diffusion, and hardening reactions of AAMs; the compressive strengths were lower in the presence of organic binders when cured at room temperature [48]. A solubility test performed by König et al. indicated a higher concentration of dissolved Si at elevated temperatures when using the hydrothermal method for GW [49]. Therefore, more gel may form during alkali activation in the case of GW, and the hardening process would be considerably slower than that in the case of SW. A combination of both is desirable because SW contains higher amounts of alumina and calcium than GW [41,50]. Our previous study showed that the presence of GW in the mixture of SW and GW improve the mechanical properties [41], and while using a mixture of both types of wool reaction is accelerated due to the presence and dissolution of more calcium from SW which affects its early strength and decreases the setting time [51]. A freeze–thaw resistance of at least 150 cycles was observed in our previous study where 33.1 wt% of SW was used in alkali-activated façade panels in addition to electric arc furnace slag, metakaolin, lime, and quartz sand activated with sodium silicate [52]. Co-binders were used to improve workability, accelerate the reaction, and increase the Si/Al ratio [51]. However, the mixture was not suitable for 3D printing because it contained sand and varied in the particle size of mineral wool used for the preparation of panels [52], which affected the extrudability (nozzle limitations) and buildability of the material produced. Additive manufacturing requires a robust mix design, as any small variation will affect the parameters for producing a suitable mixture [53]. Mineral wool is composed of microfibres that can vary in length and width after milling (the size range of microfibres is therefore important, e.g., particle size <63 µm), and it can act as a binder or reinforcement (unreacted fibre) in the structure of AAMs.

The current study presents the use of mineral wool (both SW and GW) in an alkali-activated mixture for 3D printing. This mixture includes the incorporation of co-binders such as bottom ash (BA), calcium aluminate cement (CAC) and microsilica (Mic) to improve the overall composition. It appears that no previous research has investigated the incorporation of mineral wool in 3D printing and the behaviour of such mixtures at elevated temperatures, which is the novelty of this investigation. The research goes beyond 3D printing as it expands the scope to include moulded samples, which allows for a comprehensive analysis of material properties during the curing process and includes analyses at both room temperature and elevated temperatures. In addition, the study of the behaviour of the samples under elevated thermal conditions allows an evaluation of the applicability and performance of this material for different purposes.

Table 1
Chemical composition of precursors used for preparing 3D-printed AAMs. Loss on ignition (LOI) was measured at 950 °C for all precursors except SW and GW.

m% (wt%)	GW	SW	BA	CAC	Mic
SiO ₂	58.9	38.9	27.5	0.13	84.8
Na ₂ O	12.8	1.73	0.93	0.44	0.37
Al ₂ O ₃	5.66	18.2	9.57	81.4	0.60
K ₂ O	0.38	0.89	2.09	0.01	0.86
Fe ₂ O ₃	0.90	6.24	8.90	0.09	0.68
CaO	8.96	16.7	18.9	14.6	4.15
MgO	5.24	10.9	6.84	0.19	1.54
SO ₃	0.62	0.09	2.11	/	0.02
LOI (950 °C)	5.67 ^a	4.17 ^a	21.5	2.90	6.59

^a LOI measured at 550 °C due to pure glass wool melting at 950 °C and the oxidation of the stone wool.

2. Materials and methods

2.1. Materials

Precursors used for alkali activation: All precursors used for preparing AAMs are presented in Table 1 along with the chemical compositions of the materials. Sodium silicate (Geosil 34417, Woellner, $\text{SiO}_2:\text{Na}_2\text{O} = 1.68, 55.6 \text{ wt}\% \text{ H}_2\text{O}$) was used as the alkali activator. The mix design selected for preparing 3D-printed and moulded mixtures comprised 20.8 wt% stone wool (SW, Knauf Insulation, waste material), 20.8 wt% glass wool (GW, Knauf Insulation), 6.5 wt% bottom ash (BA, waste material), 12.5 wt% calcium-aluminate cement (CAC, Samson Kamnik), 2 wt% microsilica (Mic, Samson Kamnik), and 37.4 wt% liquid sodium silicate.

Particle size distribution: Particle size distributions were measured in all five precursors prepared for alkali activation (Microtrack Sync, USA, Pennsylvania). The particle sizes of the precursors used are listed in Table 2.

2.2. Sample preparation (moulded and 3D printed)

Preparation of precursors: GW and SW (10 kg) were milled in a concrete mixer for 3 h using steel balls of different sizes (30, 40, and 47.5 mm). The sample was homogenised and then dried in a drying oven at 105 °C for 24 h before being sieved through a mesh with openings of 63 µm. The residue was ground again in a homogeniser (powder mixer shaker, Turbula T2F) using a 2 l plastic container and 50 steel balls (diameter = 9.8 mm), and sieved to below 63 µm. The final powder was homogenised. Mic and CAC were used as received, whereas BA was milled and sieved to below 63 µm.

Preparation of selected mix design: All premixed and homogenised dry precursors were placed in a container and mixed with liquid sodium silicate. Then, the mixture was mixed in an overhead mixer (Tehtnica, Železniki) at 500 rpm for 5 min. Once the paste was homogeneous and workable, the mixture was placed in silicone moulds (80 mm × 20 mm × 20 mm; moulded samples). For the 3D-printed samples, the paste was inserted into a dosing cylinder and prepared for extrusion. All samples were cured at constant temperature and relative humidity (20.5 °C ± 0.5 °C and 50–55 %). In the following text labelled as room temperature.

2.3. Methods

The AAM prepared primarily from SW and GW was tested for potential use in 3D printing. 3D printing was performed using a commercial 3D printer with certain modifications for the study. The most suitable mix design was selected by experimenting with various alkali-activated mixtures. An optimal mix design for 3D printing was developed using a heuristic trial-and-error approach.

3D printing: The printer (Delta Wasp 4020 3D-printer, Fig. 1a) used in the present study has a pressurised feeding chamber from which the material is pushed to the printhead (Fig. 1b and c). The printhead consisted of an extruding screw with a programmable speed controller. The volume of the extruded mass was regulated by the pressure in the feeding chamber and the rotation speed of the extruder screw. The extruding screw was mixed with the material before deposition. The printing area had a diameter of 200 mm and a height of 400 mm. The

Table 2

Particle size distributions with percentages of the precursors measured by passing d10, d50 and d90.

% passing	GW (µm)	SW (µm)	BA (µm)	CAC (µm)	Mic (µm)
d ₁₀	3.73	5.67	1.29	1.07	4.45
d ₅₀	13.8	24.9	8.27	17.8	32.4
d ₉₀	66.3	65.9	59.1	86.3	96.4

printing bed (Fig. 1d) was heated to 60 °C. The entire printer was enclosed in a chamber around which air was circulated to ensure that the temperature remains as homogenous as possible. The details of the 3D-printing equipment are provided in the supplementary material (Text S1 and Table S1).

Thermal treatment: The moulded and 3D-printed samples were thermally treated in a heating oven at 200, 300, 400, 500, 600, 700 and 800 °C. A heating programme was created for each sample wherein the temperature was adjusted to the desired temperature at a rate of 10 °C min⁻¹, and then held at that temperature for 20 min before being cooled to room temperature in the furnace.

Mechanical properties: To test the mechanical properties of the samples, the paste mixture was moulded into prisms (20 mm × 20 mm × 80 mm). The compressive and bending strengths were measured after 1, 3, 7, 14, 28, 56, and 128 days using a compressive and bending strength testing machine (ToniTechnik ToniNORM). A constant force rate of 0.05 kN/s was used. The bending and compressive strengths were measured using three prisms. After measuring the bending strength, the remaining half of the prism was used to evaluate the compressive strength.

X-ray diffraction (XRD): XRD analysis was performed between 4° and 70° at intervals of 0.0263° using an Empyrean PANalytical X-ray diffractometer (Cu X-ray source, 45 kV, 40 mA; Thermo Scientific, Thermo Electron SA, Ecublens, Switzerland) under cleanroom conditions using powder sample holders. The amounts of amorphous phase and minerals in terms of mass percentages were estimated by Rietveld refinement [54] using an external standard (a pure crystal of Al₂O₃) and X'Pert Highscore plus 4.1 software (version 4.1, Malvern Panalytical, Surrey, United Kingdom).

X-Ray fluorescence (XRF): For XRF analysis (Thermo Scientific ARL Perform'X Sequential XRF), powder samples were prepared in a furnace (Nabertherm B 150) and then mixed with Fluxana (FX-X50-2, lithium tetraborate 50 %/lithium metaborate 50 %) in the ratio 1:10 to lower the melting temperature. XRF analysis was performed on the melted disks using OXSAS software, and the data were quantified using UniQuant 5 software.

Fourier-transform infrared spectroscopy (FTIR): An FTIR spectrometer (PerkinElmer Spectrum Two, Kentucky, USA) equipped with an attenuated total reflection accessory (Universal ATR) was used to observe the infrared spectra of alkali-activated moulded and 3D-printed samples using a diamond/ZnSe crystal as a solid sample support in the range 400–4000 cm⁻¹ at a resolution of 4 cm⁻¹.

Vicat test: A Vicat needle was used to determine the initial setting time (and the open time suitable for 3D printing); the experiment was conducted according to EN 196–3 (Methods of testing cement - Part 3: Determination of setting times and soundness, 2008). The fresh sample was penetrated by the Vicat needle, which had a weight of 300 g and a diameter of 1 ± 0.05 mm. Penetration depth versus time was recorded with penetration readings conducted at 30-min intervals. The approximate initial setting time was recorded when a penetration of 6 ± 2 mm was achieved.

Slump test: A mixture of paste prepared for 3D printing was poured into a slump cone with a height of 75 mm and inner diameters of 38 mm at the top and 90 mm at the bottom (standard procedure EN 12350–2). The cone was placed on a smooth glass plate to minimise friction between the plate and the paste. After filling the paste, the cone was lifted slowly and the plate was shaken 15 times.

Dilatometry: A dilatometric analysis was performed using a Netzsch DIL 402 dilatometer on a sample with a height and width of approximately 7 mm and an exact length of 18.87 mm. Measurements were conducted over a temperature range of 20–700 °C at a heating rate of 5 °C min⁻¹.

Coupled Thermogravimetric-Evolved Gas Analyses (TG-MS): The thermal decomposition of the prepared samples was monitored using a Mettler Toledo TGA/DSC1 instrument connected to a Pfeiffer Vacuum ThermoStar mass spectrometer. For GW and SW, about 10 mg of the

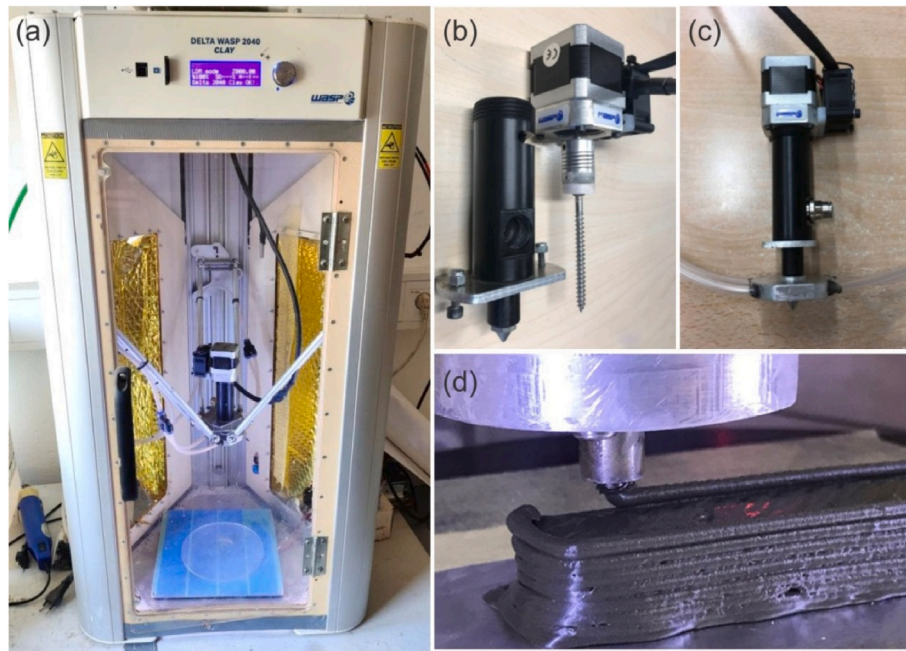


Fig. 1. (a) Delta Wasp 4020 3D printer used in the present study, (b) printhead printing for extrusion using a screw, (c) cooling the printhead with a closed loop water-cooling system, and (d) an example of printing a prism using the established printing system.

sample was placed into a 150 μL alumina crucible and heated from 25 to 950 $^{\circ}\text{C}$ at a rate of 10 $^{\circ}\text{C min}^{-1}$. The furnace was purged with air during measurement at a flow rate of 50 mL min^{-1} . An empty crucible served as reference, and the blank curve was subtracted. The evolved gases were introduced into the mass spectrometer via a 75 cm-long heated capillary. In the 3D-printed samples, the initial mass of the sample was between 4.6 and 5.6 mg, whereas the upper temperature during dynamic measurement was 650 $^{\circ}\text{C}$.

Scanning electron microscopy with energy dispersive X-ray spectroscopy (SEM-EDXS): The microstructures of the samples were examined using a scanning electron microscope (SEM, JSM-IT500LV, Jeol, Tokyo, Japan) equipped with an energy-dispersive X-ray analyser (EDXS, Link Pentafet, Oxford Instruments). Backscattered electron (BSE) detection was applied to the uncoated polished samples prepared in epoxy resin and observed under low-vacuum conditions. After measuring the mechanical strength, the nonpolished samples (sample pieces that had not been destroyed) were observed at room temperature, 200, 300, 400, 500, 600, 700, and 800 $^{\circ}\text{C}$.

Mercury intrusion porosimetry (MIP): MIP analyses were performed on the AAM samples using a mercury porosimeter (Micromeritics, Norcross, GA, USA). The samples were dried at 70 $^{\circ}\text{C}$ for 24 h before measurement and analysed using Micromeritics AutoPore IV 9500.

X-ray computed microtomography: This technique was used for the 3D visualization of samples by image segmentation and to provide quantitative information regarding internal microstructural features such as voids and pores, which influence the structural characteristics and physical properties, e.g. sample strength.

An increasing number of studies on 3D-printed AAMs have used X-ray computed microtomography (CM) to explain the pore structure and presence of cracks in the structure, thereby affecting the final mechanical properties [27,55]. Internal microstructural features and morphologies of the moulded and 3D-printed samples (20 mm \times 20 mm \times 80 mm) were determined using non-destructive, high-resolution microXCT400 (XRadia, Zeiss, Germany) equipment. Data for each sample were collected with a macro (0.39 \times magnification) lens at 140 keV acceleration voltages using a stitching mode (a process in which two volumes are merged at a common plane for creating a single volume). An

X-ray source was scanned across the entire sample, and 3D images were obtained by rotating the sample 360 $^{\circ}$. Each projection image was acquired using a 1 s exposure time and a 45 μm pixel size; 1200 images were captured in total. Following 3D tomographic image reconstruction, the commercial computer software program AVIZO Fire (*Thermo Fisher Scientific*) was used for visualizing the internal sample geometry for segmentation (Fig. 2) and quantitatively analysing the porosity, pore size distribution, and fraction of voids. Image segmentation was performed using an Interactive Thresholding tool to merge similar intensities into various image segments; in our case, the matrix, voids, pores, and cracks. 2D slices were converted from grayscale to binary images based on the selected threshold in the grey-level histogram of the image. A labelling module was used to perform a connectivity analysis of individual objects in the entire 3D volume. A filter with the measurement and sieve analysis modules was used to filter different objects, and finally, the volumes of individual pores were measured.

3. Results and discussion

A material extrusion approach was used to produce specific 3D objects (electronic components). The thermal stability of the 3D-printed products was evaluated when exposed to elevated temperatures during their service life. The first part of the results, transition temperature, and evolution of different gases were estimated using TG-MS analysis. The mechanical properties of the printed samples were examined and compared with those of the conventionally moulded AAMs, while Fourier transform infrared (FTIR) and X-ray diffraction (XRD) techniques were employed for observing the chemical and mineralogical changes induced on the hardened products because of exposure to higher temperatures or because of the curing process at room temperature. Changes in the (bulk and skeletal) density and porosity of the materials were monitored using MIP. The samples exposed to elevated temperatures were investigated using SEM-EDXS and X-ray computed microtomography.

3.1. Selecting the optimal mixture for 3D printing

A preliminary study was conducted to develop the design mix

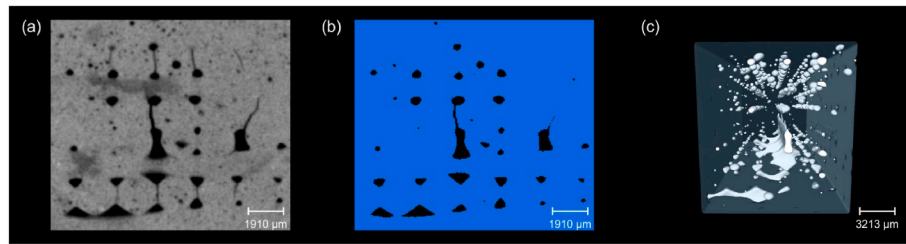


Fig. 2. Example of X-ray microtomography. (a) Grayscale 2D slice, (b) segmented image with matrix in blue, (c) segmented image of 3D volume of printed sample (segmented pores, voids, and cracks in white). (For interpretation of the references to colour in this figure legend, the reader is referred to the Web version of this article.)

investigated in the study. Several different waste materials were investigated for developing an ideal mix design for 3D printing, e.g. pulverised SW and GW, gypsum, GGBFS, FA, BA, different types of cement, metakaolin, lime, and Mic. The type of precursor used influenced the rheological behaviour (workability) of the paste, and thus, the extrusion of the prepared AAM. Extrusion is not possible when the mixture is too viscous. The mix design was modified by changing the type and amount of admixture for achieving good extrusion and shape stability with no deformation upon the subsequent loading of layers. The tested mixtures are listed in Table S2 and described in Text S2. Based on this information and our previous experience using SW and GW for AAMs [41,56], we obtained a mix design that could be extruded and retained its shape after printing (the mixture comprised of GW, SW, BA, CAC, and Mic). A long initial setting time is required to avoid premature stiffening when the mixture is extruded and printed. The initial and final setting times were 7 h and 8 h, respectively, whereas the AAM (i.e. open time) could be printed for up to 3 h (usually between 1 and 2 h). Although CAC was added to the mixture for accelerating the setting time, mineral wool, which is the predominant precursor in the mixture, exhibits low reactivity at room temperature [41], and thus, prolongs the setting time. However, slow alkali activation can self-heal defects formed during 3D-printing. The workability of the mix design was initially insufficient, and when the material was continuously added, it was difficult to mix the paste to obtain a homogeneous mixture. After mixing for 5 min, the workability of the paste improved once all of the material was wet; the slump test showed values of 158/163 mm for the selected mix design (results from a previous study suggest that the optimal workability for a mix design containing GW or SW is in the range 165–180 mm [56], lower values are desirable for 3D printing). The water-to-binder ratio of the paste was 0.33. The paste adhered to the metal of the stirrer; however, the adhesive properties and cohesion of the mixed pastes ensured good adherence to the surface, which influenced the interfacial properties (interlayer bonding in layered manufacturing affects the mechanical properties of the printed material) [57]. In a previous study by Panda et al., nano-clay was added to AAMs for improving their rheological characteristics in terms of their applicability to 3D printing [58]. Rheological parameters besides maximal viscosity and the time at which maximal viscosity was achieved are not studied in this paper. These parameters for the various mix designs tested in the present study are listed in Table S2. The alkali activation and hardening processes when using a mixture of GW and SW were slow. This was overcome by adding CAC to the original mix design for accelerating the hardening. Although CAC accelerated the hardening process, the buildability of the prepared paste was not observed (the mixture did not retain its shape after extrusion). Therefore, BA was added 1) to decrease workability and 2) improve buildability (shape retention). This mix design (with GW, SW, CAC and BA) was very viscous after preparation (torque overload; see Table S2 in the supplement). Micro-silica was added to the mixture to improve the extrusion and workability of the material. A decrease in viscosity and thixotropic behaviour was observed in the mixture when Mic was added, and this could have resulted in a lack of stability in the shape of the deposited layers. The buildability of the layers and shape

stability was improved by heating the bottom of the 3D printer to 60 °C. The test sample had sufficiently hardened after printing, and it could be manually removed from the printing plate. It hardened completely after one day of curing at room temperature.

3.2. Characteristics of the moulded and 3D-printed samples at room temperature

3.2.1. Mechanical properties

After 28 days of curing at room temperature, the average density was 1.91 kg m⁻³ for the moulded samples and it was slightly lower for the printed samples at 1.85 kg m⁻³. In the study by Chougan et al., the density of the 3D-printed samples was 2.7–2.9 % lower than that of the moulded AAMs (regardless of the precursors used) if the extruded mixtures had a lower flowability and shorter setting time. A short setting time may increase the porosity during the extrusion process and result in weaker bonding between the layers with more pores between them [35]. The densities of 3D-printed samples varied because of the printing process. More compact printing resulted in 3D-printed specimens with better mechanical properties, whereas significantly lower strength was observed in samples with lower densities.

The compressive and bending strengths of the moulded samples after 1, 3, 7, 14, 28, 56, and 128 days of curing at room temperature are shown in Fig. 3. The bending strength increased up to 128 days, reaching a maximal value of approximately 30 MPa, whereas the compressive strength was over 100 MPa after 56 days and remained similar after 128 days, indicating that the final compressive strength was achieved after 56 days.

All samples were printed without any time delay; however, the mechanical strength of the printed samples was primarily dependent on the time gap between the layers, which was further linked to the size of the sample and the printing speed [29]. A comparison between the moulded

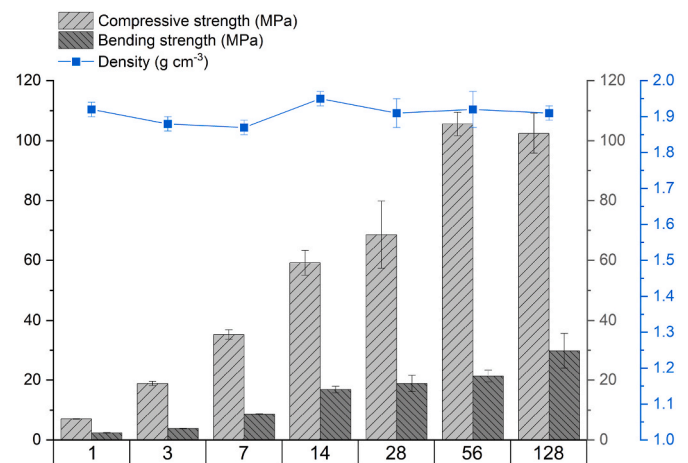


Fig. 3. Compressive and bending strengths of the moulded samples after 1, 3, 7, 14, 28, 56 and 128 days.

and printed samples was then performed after 28 days of curing, with the compressive strength of the moulded and printed samples being 68.8 and 53.7 MPa respectively, and the bending strengths being 18.8 and 12.3 MPa. After 28 days, the compressive strength in the moulded samples was 1.3 times higher than the printed samples in the present study, which is lower than that shown in the study by Bagheri and Cremona, where the compressive strength of moulded AAM specimens was 1.6–2.3 times that of layered 3D-printed samples [33]. The mechanical properties of the 3D-printed samples are not as favourable as those of the moulded samples because of their lower density (the printing increases the porosity) and the potentially weak contacts between the layers (as a consequence of the printing process, dependent on the speed of printing, freshness of the material, connection between the layers, porosity between the layers, etc.). The higher compressive strength of the moulded samples compared to that of the printed samples was attributed to the increased porosity between the layers of the printed material [32]. If the bond between the layers is not well established, large voids may exist, and this can lead to increased heterogeneity and lower compressive strength [11]. However, the properties of 3D-printed AAMs also depend on the printing parameters such as printing method, resolution of the layers, shape of extrusion (circular, oval, or rectangular), linear rates of extrusion, manufacturing orientation (vertical or horizontal), and methods of preparation and formulation [29,33]. In addition, the chemical composition of the aluminosilicate raw materials (i.e. the precursors), type of alkali activator, content of alkaline ions in the activator, ratio of silicate to hydroxide compounds in the activator, water-to-binder ratio, and type of aggregate are important factors that need to be considered with respect to the mechanical properties of the printed AAMs. The direction of printing is also important because the compressive strength in the x-direction is higher than that in the y- and z-directions [29,59]. The fibres used in the mix design for 3D printing decrease the bending strength because of a weaker bond strength between the layers caused by insufficient aluminosilicate bonds between the layers of the matrix and reduce the time gaps between subsequent layers, whereas the increased thickness enhances the bending strength [60]. In the present study, the addition of GW and SW played an important role in improving the mechanical properties (especially the bending strength) because the fibres did not completely dissolve during alkali activation [41]. Therefore, they enhanced the mechanical properties of the prepared alkali-activated material, regardless of whether they were printed or moulded.

3.2.2. XRD

The XRD patterns of the precursors and moulded AAMs cured at room temperature are shown in Fig. 4. When cured at room temperature, no difference was observed in the mineralogical compositions of the samples after 3 or 128 days of curing. Examining the XRD patterns of GW, SW, BA, CAC, and Mic indicated that most crystalline peaks found in the precursors were also present in AAM (although the peaks had lower intensities because of dilution). Following alkali activation, GW, SW, and Mic contain more than a 90 % amorphous phase, showing a broad hump that shifts slightly towards higher 2θ values. However, the presence of a broad hump ('halo') produced between 2θ values of 26° and 36° indicates the presence of the alkali-activation process [61]. The amorphous contents of the precursors, AAM, and goodness of fit, as determined by Rietveld refinement, are shown in Table 3. The major crystalline phases found in the precursors and AAMs are shown in Fig. 4.

3.2.3. TG-MS

Fig. 5a shows the TG-MS results for the GW and SW samples between room temperature and 950 °C. Weight loss was higher in GW (5.54 %) than that in SW (4.04 %) over the entire temperature range, which is consistent with the LOI shown in Table 1. In SW, oxidation and a consequent increase in mass is observed between 530 °C and 850 °C. A slight increase in mass also occurred in GW (0.13 % increase between

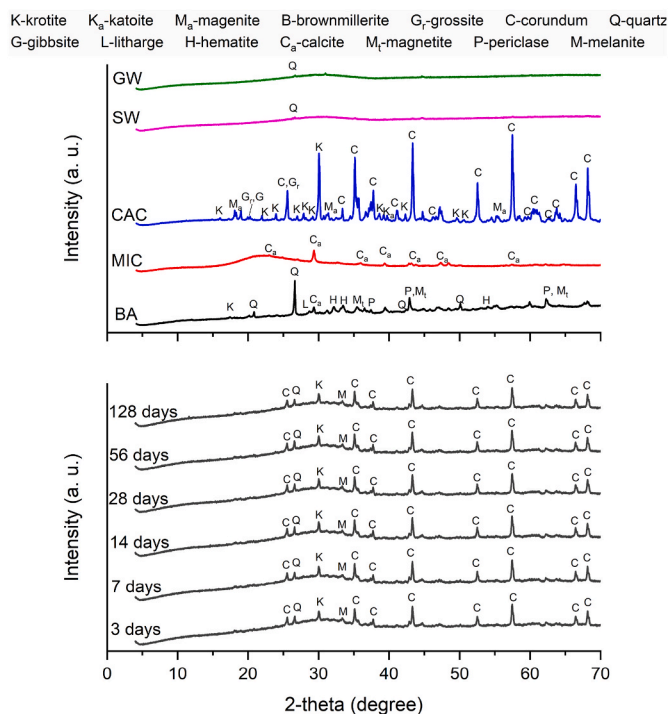


Fig. 4. XRD diffractograms of the precursors used in the selected mix design (GW, SW, CAC, Mic, and BA) and the alkali-activated paste cured at room temperature. Measurements were performed after 3, 7, 14, 28, 56, and 128 days.

Table 3

Percentage of amorphous phase and goodness of fit for the precursors and AAMs determined by Rietveld refinement.

	Amorphous phase (%)	Goodness of fit
GW	99	5.7
SW	99	5.0
Mic	94	10.3
CAC	13	5.8
BA	64	5.7
AAM 3 days	86	5.7
AAM 7 days	86	5.6
AAM 14 days	86	5.8
AAM 28 days	86	5.7
AAM 56 days	87	6.0
AAM 128 days	86	5.4

560 °C and 850 °C). The ion current shown on the right axis in Fig. 5a indicates the release of water ($m/z = 18$), CO_2 ($m/z = 44$), and SO_2 ($m/z = 44$). The first step in the TG curve (from room temperature to 200 °C) is related to the release of water, whereas in the second step (from 200 °C onwards), water, CO_2 , and SO_2 are evolved. The evolution of CO_2 completes at around 500 °C in SW and 550 °C in GW. Differences in the end set temperature and ion current signal profile indicate a difference in the decomposition pattern of organic compounds in the precursors, which is the main reason different binders cover the SW and GW fibres [45]. The release of SO_2 is more intensive in GW, which is in accordance with the amount of SO_3 measured by the XRF analysis, as shown in Table 1. The TG curves of the remaining precursors (BA, Mic, and CAC) and the CO_2 evolution during heating are presented in Fig. 5b. The intense CO_2 signal in BA between 250 and 550 °C at $m/z = 44$ most likely corresponded to unreacted carbon particles. It is assumed that the decomposition of CaCO_3 starts above 600 °C in BA, as shown by the steep curve in Fig. 5b [62] the signal for CO_2 also increases. However, this decomposition was not followed up to 800 °C [63] because in our case, measurements were only performed up to 650 °C. In Mic, CO_2

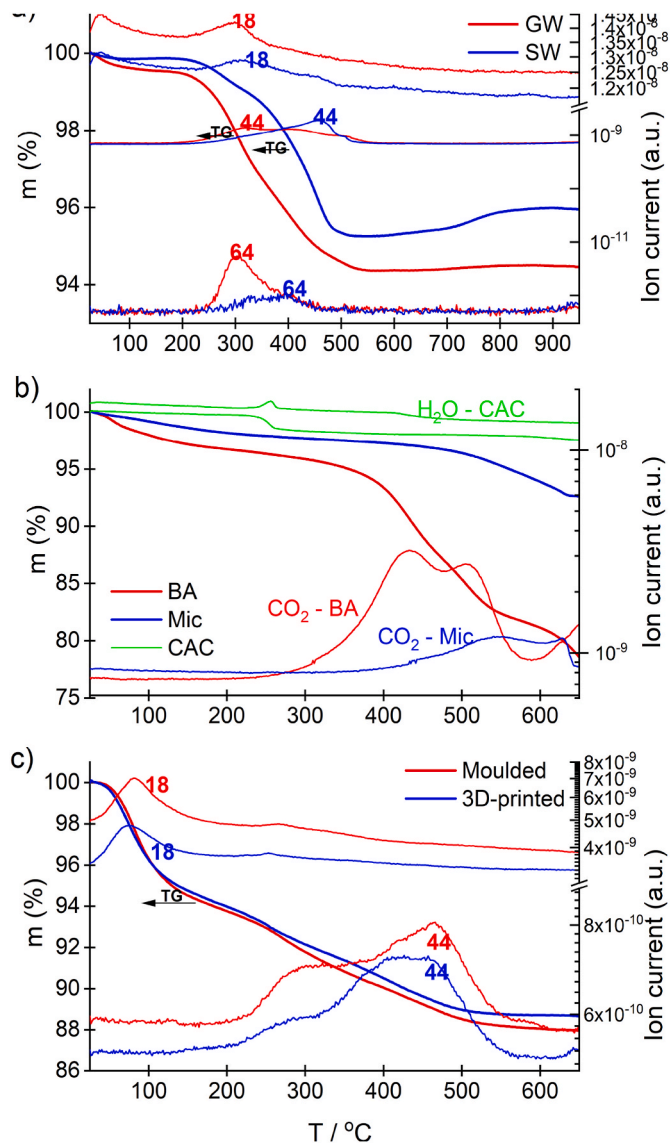


Fig. 5. (a) TG-MS curves of GW and SW. The left axis indicates the mass loss of the samples when heated in a dynamic air atmosphere, while the right axis indicates the ion currents of CO_2 ($m/z = 44$), SO_2 ($m/z = 64$), and H_2O ($m/z = 18$) released from the samples. (b) TG-MS curves of BA, Mic, and CAC, and the evolving gases H_2O ($m/z = 18$) and CO_2 ($m/z = 44$). (c) TG-MS curves of the AAM (moulded and 3D-printed). The left axis indicates the mass loss of the samples when heated in a dynamic air atmosphere, while the right axis indicates the ion currents of CO_2 ($m/z = 44$) and H_2O ($m/z = 18$) released from the samples.

evolves between 400 and 650 °C because of the thermal decomposition of CaCO_3 [64]. A small release of water ($m/z = 18$ (H_2O)) was observed in CAC between 220 and 265 °C, indicating dehydration.

Fig. 5c shows the TG-MS curves of the moulded and 3D-printed AAM samples. The large weight loss between room temperature and 150 °C (approximately 5 %) corresponds to the loss of physisorbed water from the AAM. The additional small peak of water at around 250 °C results from combustion of organic material. A release of CO_2 was observed between 250 and 550 °C, most probably because of the decomposition of the organic binders in GW and SW and the unburned carbon in BA.

3.2.4. FTIR analyses

Fig. 6 shows the FTIR spectra of the powdered precursors (CAC, BA, Mic, GW, and SW) used in the present study. The CAC sample shows several spectral features in the fingerprint region at 635, 583, 492 cm^{-1} ,

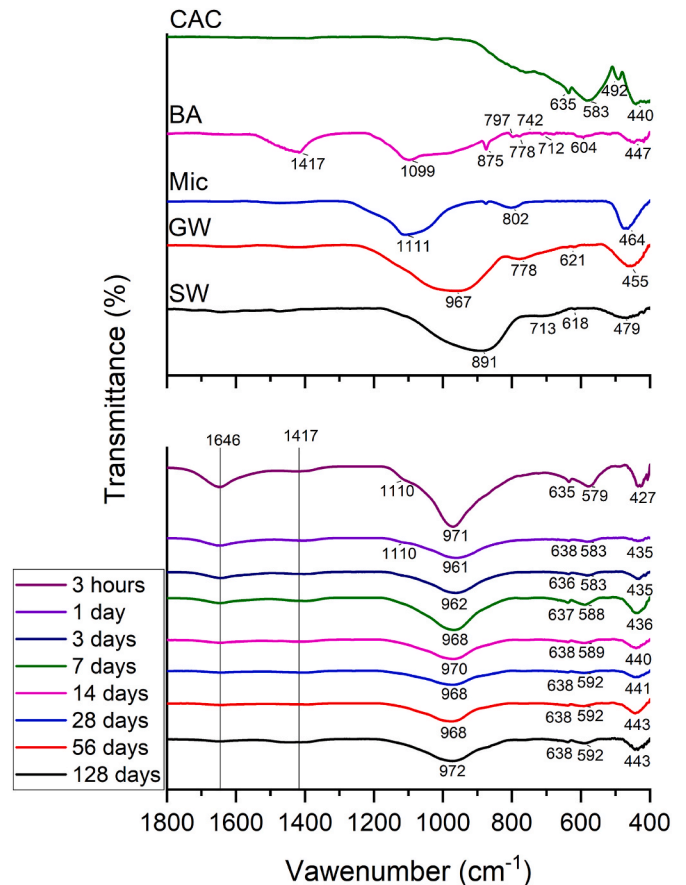


Fig. 6. FTIR spectra of the precursors and alkali-activated mixtures (moulded samples) cured at room temperature after 3 h, 1, 3, 7, 14, 28, 56, and 128 days.

with many small peaks at around 440 cm^{-1} . The aluminate-oxygen stretching bands positioned between 700 and 920 cm^{-1} represent tetrahedrally coordinated aluminate with oxygen (the bands are barely visible) assigned to condensed AlO_4 tetrahedra and isolated AlO_4 tetrahedra [65]. The bands at approximately 718, 635, and 583 cm^{-1} are associated with the AlO_6 octahedral units in the structure [66]. The peak at 440 cm^{-1} is attributed to the bending vibrations of the Al–O–Al bonds [65]. The bands at 1099 cm^{-1} in BA indicate the asymmetric stretching vibration of the Si–O–Si group, whereas those at 797 and 778 cm^{-1} show the Si–O–Si symmetric stretching vibrations of quartz present in the sample [67,68]. The presence of peaks in the fingerprint region at 712 and 875 cm^{-1} indicate the presence of calcium carbonate in the sample, whereas a weak shoulder at ~ 875 cm^{-1} is attributed to the out-of-plane bending of CO_3^{2-} [69]. The Mic used in the present work exhibited three peaks: the first two peaks were centred at 464 cm^{-1} and 802 cm^{-1} , and a third broad peak was observed at 1111 cm^{-1} . The most intensive, broad peak, observed at 1111 cm^{-1} , represents the asymmetric stretching of silicon atoms in siloxane bonds. The symmetric vibrations of the silicon atoms in the siloxane Si–O–Si bond occur at 802 cm^{-1} [70], whereas the peak at 464 cm^{-1} is assigned to the Si–O bending vibration [71]. The SW and GW mineral wool samples show a broad band (indicating a disordered silicate structure) that corresponds to the asymmetric stretching vibration band of Si–O–T (T = Si or Al) present at 891 cm^{-1} in SW and at 967 cm^{-1} in GW. A broad band was positioned at a lower wavelength. In SW, this indicates more Al–O and Al–O–Si bonds in the vitreous phase than in the GW sample (in accordance with the chemical composition shown in Table 1). In GW, the band at 778 cm^{-1} indicates a Si–O band (in the SiO_4 tetrahedron) [72]. In SW, a band observed at 666 cm^{-1} is attributed to the symmetrical stretching of Si–O–T [73].

AAMs results from the reaction of aluminium-silicate materials in a strongly alkaline environment, where Si–O–Si bonds are broken down in the precursor and a new phase is formed. This is clearly observed in Fig. 6, where the most intensive band, in the range $961\text{--}972\text{ cm}^{-1}$, represents the asymmetric stretching of Si–O–Si. A transmission band at approximately 1645 cm^{-1} indicates the presence of an H–O–H bending vibration caused by water which was either present in the initial mixture or adsorbed at the surface of the waste. However, after 14 days, this peak was no longer observed. During the dissolution step, the Al–O–Si and Al–O–Al bands in the amorphous phase were broken more readily than the Si–O–Si bands, resulting in weaker bonds between the network-forming and network-modifying species [74,75]. Therefore, an Al-intermediate reaction product prevailed at the start (FTIR spectra after 1 day); however, as the reaction progressed, more Si–O groups became available from the precursors and were replaced with Al. This can be observed in the asymmetric stretching of Si–O–T (T = Si, Al), which shifts to higher frequencies. However, after 28 days, there was a slight shift to higher frequencies, as indicated by the higher compressive strengths and increased number of Si–O–Si bonds [76]. Bands at approximately 635 cm^{-1} and between $579\text{ and }592\text{ cm}^{-1}$ are associated with the tetrahedral aluminosilicate system and are characteristic of double-/single-ring and/or TO_4 (T = Si, Al) tetrahedral bonds. The formation of three-dimensional structures because of the ring interconnections generates variations in the number, shape, and position of bands between $500\text{ and }800\text{ cm}^{-1}$ [66]. The higher reactivity of the SW precursor in alkali is indicated by the more intense shift of the band compared to that of the GW samples. The position of the Si–O–T (T = Si, Al) band shifts from 971 cm^{-1} at 3 h, when the processes of dissolution and alkali activation occur, to 961 cm^{-1} after one day, when the AAM solidifies and alkali activation continues to progress. The band at approximately 1110 cm^{-1} was still observed after one day; however, it disappeared after three days. Narrowing of the peak was observed in all AAMs because of the more condensed tetrahedral species [77]. After 14 days, most of the reaction process was completed (there was no more water in the samples, as seen in Fig. 6), and the compressive strength reached approximately 60 MPa. However, alkali activation and reorganisation of the structure continued until 128 days, as confirmed by the improvement in mechanical properties.

3.2.5. X-ray computed microtomography

Microstructural evolution was investigated in the moulded samples cured at room temperature (T_0). The visual observation of microtomography results revealed the formation of microcracks (Fig. 16). The paste was stirred during preparation to evenly disperse the particles. The

blades of the mixer were rotated at a high speed, and a low-pressure zone formed near the blades, enabling air to be incorporated into the paste. The rate at which air escapes from the paste is affected by its viscosity; it is more difficult for air to escape when the viscosity is higher [78]. During the paste curing process, air moves upward, and some air is released, whereas some forms isolated air voids, as shown in Fig. 16.

To produce dense 3D-printed parts, the right balance between shape retention (buildability) and viscosity should be identified because shape retention is strongly dependent on the nozzle diameter, layer height, and width. The latter is influenced by the extrusion rate and print speed, and these printing parameters have a large impact on the extruded material, which should flow sufficiently to fill the void spaces between stacked cylindrical layers (filaments). Another critical parameter affecting the density of 3D-printed parts is the drying process, which can cause issues such as warping, pore coalescence, crack development, and shrinkage [79]. These parameters can only be determined using non-destructive X-ray computed microtomography.

The size and distribution of the void spaces and pores is shown in the histogram of the 3D-printed sample cured at room temperature (Fig. 7; not exposed to elevated temperatures; hereafter referred to as ‘3D-printed sample T_0 ’). To obtain such results and visual representation, pores and voids were divided into three categories (inter-filament voids, macropores, and micropores, based on a previously reported method [80,81]), which are schematically illustrated in Fig. 7 to help the reader visualise their location in the 3D-printed sample.

The histogram in Fig. 7 shows that most voids and pores are up to 1.25 mm in size. Voids larger than 1.2 mm in diameter represent the largest interfilament voids and can be seen in the middle of the sample (Figs. 7–8a). Such voids can be located between the stacked cylindrical filaments of the surrounding layers present weak interconnections between the layers and the rectangular grid of the printing pattern in the cross section. These voids can also be defined as macrochannels (formed between different semi-circular filaments in the cross section). Large voids or channels are aligned along the filament in the y-axis direction. Their length varied from a few millimetres to the entire length of the sample (in our case, the largest void was 4.5 cm) and was typically wide, between 1 and 1.5 mm. This indicates that the viscosity was sufficiently high for the filaments to retain their slightly elliptical shape and prevent the spaces from being completely filled. This should be noted because of the importance of free void spaces during sintering, which influence the overall density and cracking of the sample [78].

Further, larger voids can be observed at the bottom and on the side surfaces of the sample (Fig. 8b), which can be caused by nonhomogeneous and unintentional printing and inhomogeneous drying (the

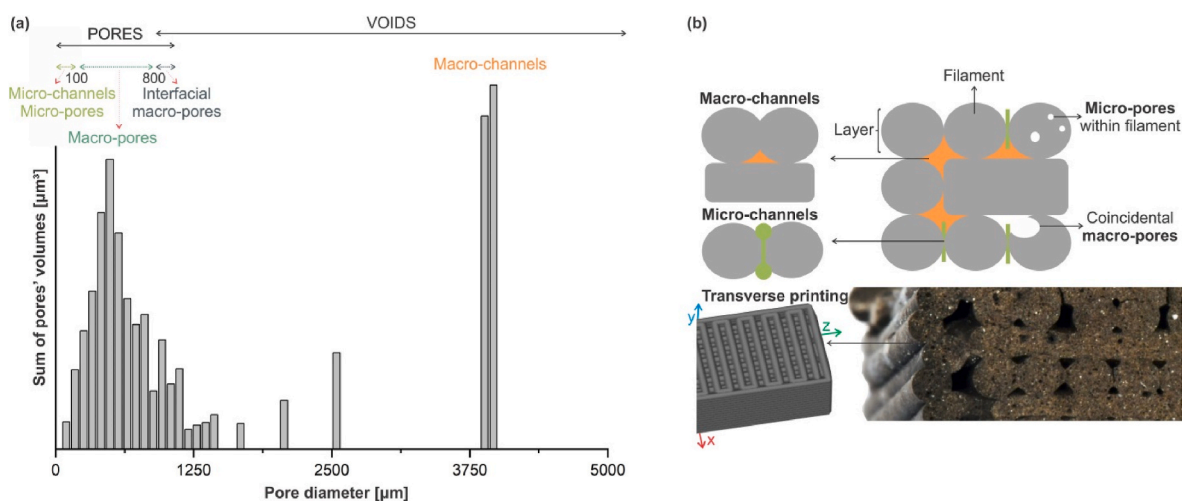


Fig. 7. (a) Pore size distribution presented as the volume of pores/voids with respect to the pore size diameter, as determined by X-ray computed microtomography, and (b) a schematic representation of the printed filaments showing the cross-sections of different categories of air pores and voids.

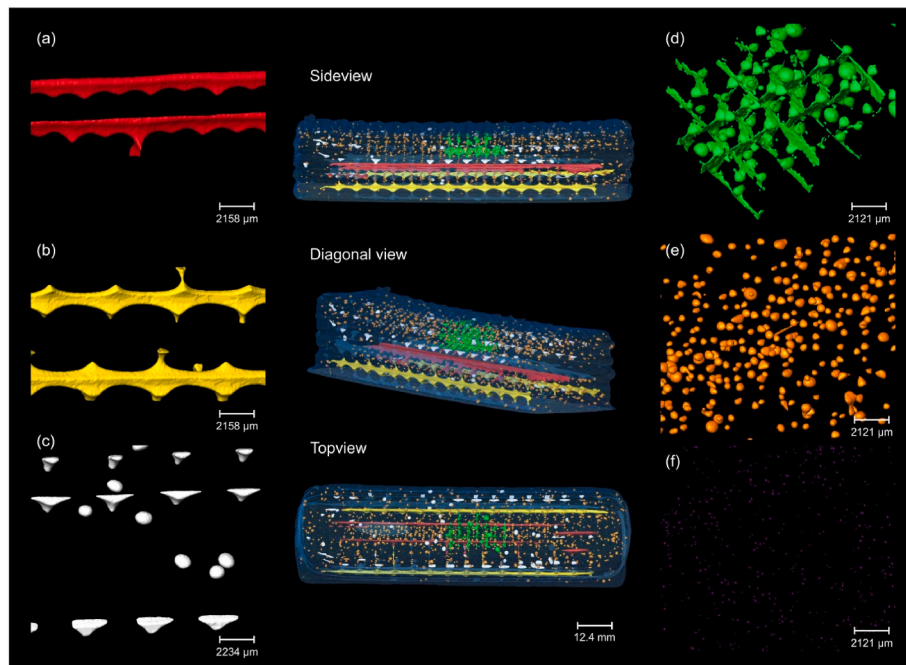


Fig. 8. Visual presentation of voids and pores in the non-sintered 3D-printed sample obtained by X-ray computed microtomography, showing (a) inter-filament voids, (b) bottom voids, (c) interfacial macro-pores, (d) micro-channels (the 10 largest in the defined ROI for easier visualization), (e) macro-pores (diameter between 400 and 800 μm), and (f) micro-pores.

heating plate is positioned at the bottom of the 3D printer and is in constant contact with the bottom layer of the sample) because of the presence of a closed surface at the bottom caused by the evaporation of water and particles on the open surface [79]. The width of the voids at the bottom surface was approximately 1.1 mm, with lengths varying from 5 to 6 cm. These dimensions correspond to estimated volumes of 47 mm^3 and 57 mm^3 . The shape is rectangular and corresponds to the characteristics of macro channels.

Another group of larger inter-filament voids (between 0.8 and 1.2 mm in diameter) formed between semi-circular filaments have a triangular shaped cross-section (when viewed along the axes of the filaments) in one direction, as seen in Fig. 8c. Moini et al. (2018) suggested that the rearrangement of filaments and the accumulation of anhydrous cement grains (in cement-based materials) near macropores are responsible for forming these triangular gaps [80]. In this study, these macropores are defined as interfacial macropores. At certain locations, these filaments are rounded or even assume the shape of a water drop.

A different microstructure is observed in the 3D-printed sample (T_0). The micro-channels are voids present at the interface between two adjacent filaments oriented along the length of the filaments (Fig. 8d). These channels were connected to the interfacial macropores on both sides. The micro-channels of cement-based materials [81] had a width and height of up to 100 μm . In this study, the size of the channels varied based on the height of the filament, which changed according to the size of the interfacial macro pores and the connection between them, ranging in width from 50 to 100 μm and the pore volume from 0.5 to 16 mm^3 .

Voids smaller than 0.8 mm in diameter represent macropores (Fig. 8e), and such pores are considered isolated pores located randomly throughout the sample. These pores were also the most common pores in the sample, according to the histogram (Fig. 7). The micro-pores are smaller than the micro-channels (Fig. 8f; diameter below 100 μm that were still identifiable at resolutions achievable by 0.4X magnification). Further, micro-pores are present in the bulk of the material within the filaments.

The results show that the 3D-printed sample (T_0) contained small cracks primarily caused by dehydration during the curing process. Inhomogeneous drying was observed during curing, which caused slight

warping (Fig. 8).

3.3. Results from the characterisation of the moulded and 3D-printed samples thermally treated at elevated temperatures

3.3.1. Dilatometric study

To analyse the thermal stability of the specimens, a dilatometric analysis was performed up to the temperature at which a significant change was observed. Fig. 9 shows the dilatometric curve of the moulded AAM sample. The curve shows that the sample shrank between 100 and 200 $^{\circ}\text{C}$; the first derivative confirmed peak occurred at approximately 127 $^{\circ}\text{C}$ and the second at 177 $^{\circ}\text{C}$, which can be ascribed to the dehydration of free water. Slight thermal shrinkage was expected in the FA-based AAM between 300 and 600 $^{\circ}\text{C}$ because of the physical contraction caused by the release of hydroxyl groups [82]; this was noticed in our study. Significant shrinkage was observed in the FA-based

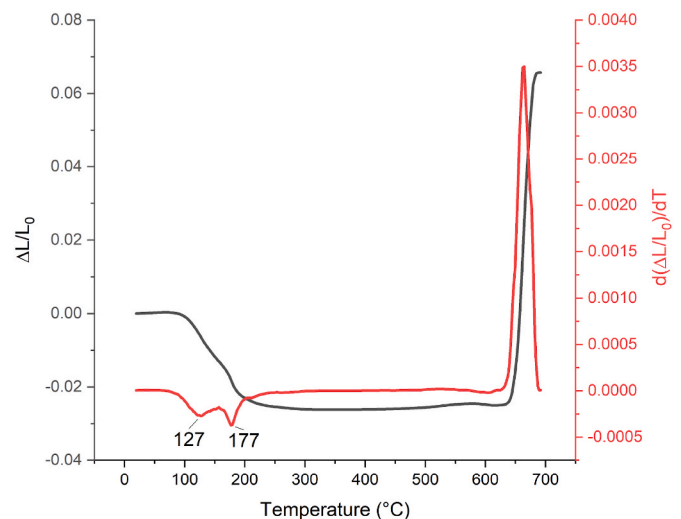


Fig. 9. Dilatometric curve of the moulded AAM.

AAM above 600 °C, and it was attributed to vitreous sintering densification. However, in our case, the sample expanded significantly above 630 °C. This can be caused by the reaction of sodium silicate and the decomposition of carbonate, which creates pores that become trapped in the structure in an already softened glassy matrix [83]. After the first shrinkage between 100 and 200 °C, the sample exhibited geometrical stability up to 600 °C. Then, a microstructural analysis was performed after the thermal treatment of the samples at temperatures between room temperature and 800 °C.

3.3.2. Mechanical properties

Fig. 10 shows the bending and compressive strengths of the moulded and 3D-printed samples after curing at room temperature (T_0) or following thermal treatment at 200, 300, 400, 500, 600, 700, or 800 °C. Dilatometric analysis (Fig. 9) showed the expansion at around 630 °C, and the highest testing temperature did not exceed 700 °C. The compressive strength of moulded samples cured at room temperature was approximately double that of the 3D-printed samples, which indicates the effect of printing and composing the samples from the layers. The bending strength of 3D-printed samples is higher not only at room temperature but also at elevated temperatures, except at 300 °C, where a high standard deviation of measurements was obtained. The decrease in the compressive strength at 200 °C can be attributed to the evaporation of free water from the pores, which causes slight structural changes and cracks in the sample during dehydration [84]. Cracks were observed in both the moulded and 3D-printed samples. At 300 °C, the decomposition of organic compounds and evaporation of bound water and CO_2 resulted in a significant decrease in the compressive strength in the moulded samples; however, this was not the case for the 3D-printed samples (Fig. 10). At 300 °C, the 3D-printed samples exhibited a compressive strength similar to that of the samples at 200 °C, and the bending strength was lower. It was found that dehydration of capillary water caused cracking and strength losses at temperatures ≤ 300 °C. Thermal

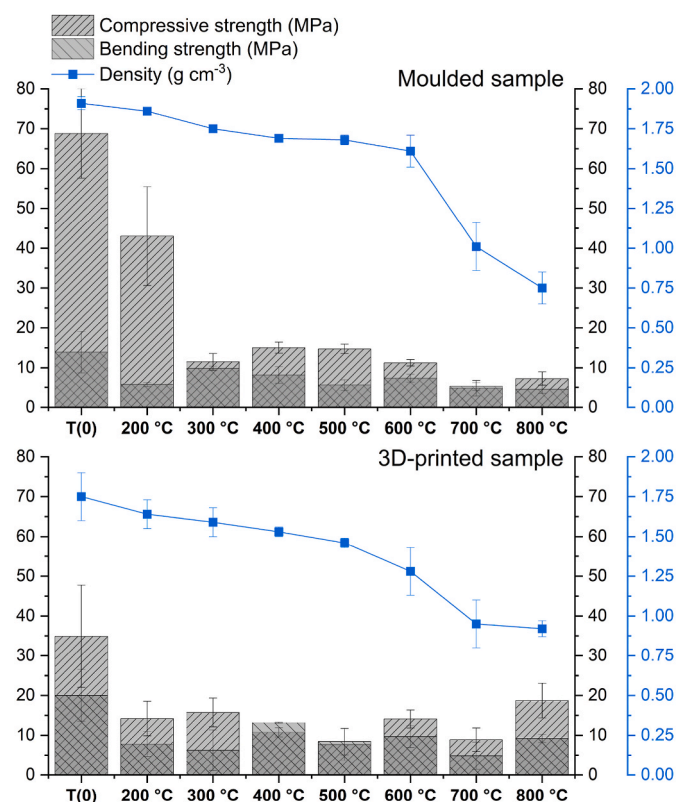


Fig. 10. Density and mechanical properties of the moulded and 3D-printed samples subjected to thermal treatment.

treatment at elevated temperatures (>300 °C) promoted crack healing in the samples, allowing AAM to regain strength following the significant cracking caused by dehydration at lower temperatures [84]. This was particularly true for the 3D-printed samples, which showed a slight improvement in the mechanical properties, but not in the moulded samples, which showed a significant decrease in the mechanical properties. The decomposition of the organic binder started at about 250 °C, as observed by TG-MS (Fig. 5), and CO_2 evaporated more easily in the 3D-printed structure than that in the moulded samples. This hindered crack healing in the moulded samples, leading to the additional destruction of the structure and the deterioration of mechanical properties. At 400 and 500 °C, the mechanical properties of the moulded samples remained similar; however, they were reduced in the 3D-printed samples. At 400 °C, a slight improvement in compressive strength was observed in the moulded samples, which increased the bending strength of the 3D-printed samples. At higher temperatures ($T \geq 500$ °C), sintering promoted an increase in strength, giving the AAMs a significant strength advantage over conventional materials [84]. An increase in compressive and bending strength was observed in the 3D-printed samples at 600 and 800 °C compared with that at 500 °C; however, this was not observed in the moulded samples (printed samples have empty spaces in the structure because of the printing model, which means that the gases were released rather than trapped in the matrix, decreasing the mechanical strength in moulded samples). Although dilatometric analysis determined that expansion occurred at 630 °C, a slight expansion was observed at 600 °C in both the moulded and 3D-printed samples. Moreover, a greater expansion was observed in the moulded samples treated at 700 °C, where a decrease in mechanical properties was observed in both moulded and 3D-printed samples. However, at 800 °C (Fig. 10), the mechanical properties of the moulded samples increased slightly compared to those at 700 °C, and a significant increase was observed in the 3D-printed samples.

The geometrical densities of the moulded and 3D-printed samples decreased after exposure to elevated temperatures, reaching the lowest values at 800 °C, i.e., when the samples were deformed and the structure became inflated. Sample bloating was observed in the moulded samples after treatment at 300, 400, and 500 °C, wherein the organic material decomposed and gases were released. The density of the sample decreased slightly up to 600 °C, and then at 700 and 800 °C, a steep decline was observed in the moulded samples because of the expansion of the sample (expansion of the moulded samples at 800 °C was approximately 105 %, compared to approximately 58 % in the 3D-printed samples; examples of the moulded and 3D-printed samples before and after exposure to a temperature of 800 °C are shown in Fig. 11). A decrease in density was also observed in the 3D-printed samples at 600 °C. The densities of the samples differed at the same temperature; it was lower in the 3D-printed samples because of the printing method and the pores between the layers (i.e. its lattice structure).

3.3.3. XRD analyses of samples exposed to thermal treatment

X-ray diffraction patterns of the moulded samples exposed to elevated temperatures were obtained and compared with the reference T_0 samples (XRD patterns for the 3D-printed samples are provided in Fig. S2). Till 700 °C, the amount of the amorphous phase (according to Rietveld refinement) was approximately 86 % in both the moulded and 3D-printed samples, as shown in Table 4. The amount of amorphous phase showed a significant drop (to 46 %) at 800 °C, which is consistent with the XRD patterns shown in Fig. 12, where new and different phases, including nepheline, diopside, and akermanite-gahlenite, can be seen. At 800 °C, a broad hump indicating AAM with a peak between 26° and 36° (2-theta) disappeared. Changes in the mineralogy of the AAM also affected the structure of the thermally treated synthesised material. For example, at 700 °C, the decrease in mechanical properties was attributed to the expansion and lower density of previously formed AAMs compared to that at 600 °C (Fig. 10). The improvement in mechanical

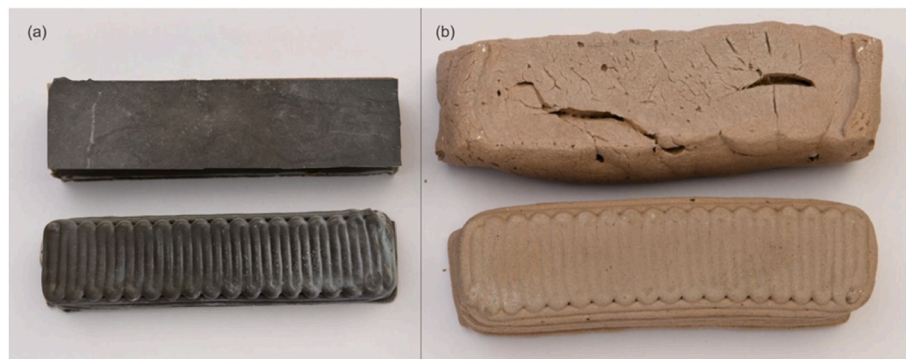


Fig. 11. Moulded (above) and 3D-printed (below) samples before (a) and after exposure to 800 °C (b).

Table 4

Amount of amorphous phase (wt%) in the moulded and 3D-printed samples before and after thermal treatment.

	Amorphous phase (%)	Goodness of fit
AAM-T ₀	86	5.9
AAM-T ₀ (printed)	85	5.4
AAM-200 °C	85	5.5
AAM-200 °C (printed)	87	5.3
AAM-300 °C	86	5.4
AAM-300 °C (printed)	84	5.3
AAM-400 °C	86	5.4
AAM-400 °C (printed)	85	5.2
AAM-500 °C	86	5.3
AAM-500 °C (printed)	85	5.1
AAM-600 °C	85	5.0
AAM-600 °C (printed)	83	4.9
AAM-700 °C	85	3.7
AAM-700 °C (printed)	87	4.0
AAM-800 °C	46	5.2
AAM-800 °C (printed)	46	4.9

properties at 800 °C could be related to the formation of new mineralogical phases.

3.3.4. FTIR analyses of the thermally treated samples

The FTIR analysis results of the moulded samples, shown in Fig. 13, indicate a slight degradation in the chemical structure of both types of samples following exposure to elevated temperatures (FTIR analyses of the 3D-printed samples show similar results, as shown in Fig. S2). The main asymmetric stretching band starts to broaden, and a minor shift in the position of the peak to lower wavenumbers indicates that the AAM is stable up to 700 °C, consistent with the XRD mineral phases (Fig. 12). Heating the material causes structural disorder, which results in broadening of the main Si–O–T band (T = Si, Al). The decrease in the wavenumber is attributed to the lower extent of polymerization in the matrix [85] and a decrease in network connectivity [86], which is most probably a consequence of structural changes and the evaporation of water, CO₂, and other gases from the structure, as proven by the TG-MS analysis. The bands at around 776 cm⁻¹ could be attributed to the presence of Si–O–Si and O–Si–O bonds in various configurations as part of the AAM network [72,87]. Till 300 °C, the shifts to lower frequencies were only minor, whereas the shifts in Si–O–T (T = Si, Al) were higher at higher temperatures. Finally, at 800 °C, new bands were observed in both the 3D-printed and moulded samples. This is consistent with the results of XRD (Fig. 12), where new mineralogical phases were shown to occur at 800 °C, e.g. napheline appeared as a newly formed phase at around 695 cm⁻¹, and as a weak shoulder at 1081 cm⁻¹.

3.3.5. Hg-porosity of the thermally treated samples

The pore size distribution of the moulded AAMs, measured by MIP between 0.003 and 339 μm, is shown in Fig. 14; porosity is indicated as a

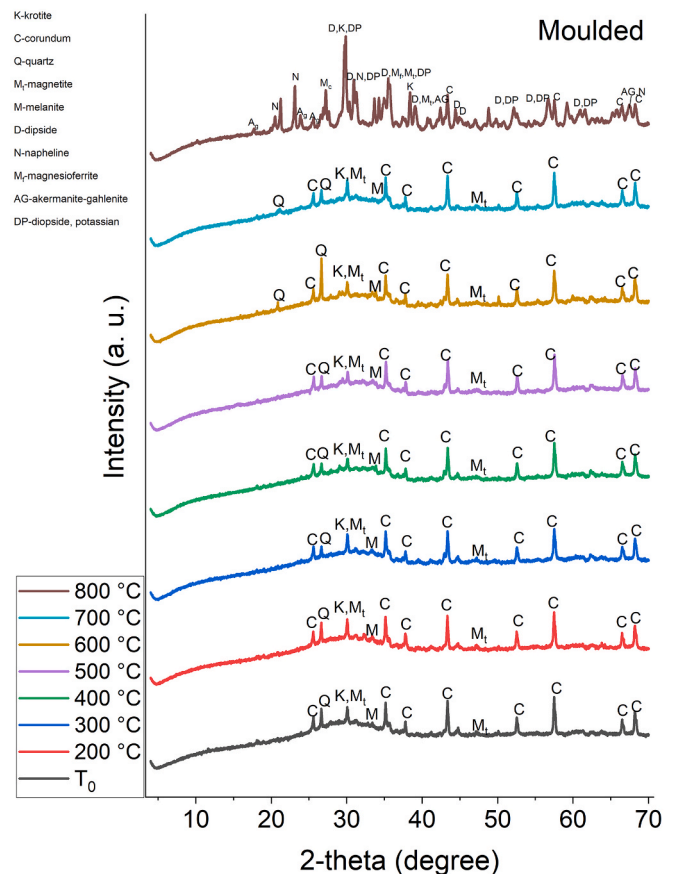


Fig. 12. X-ray diffraction patterns of the moulded samples exposed to elevated temperatures and the samples cured at room temperature (T₀) as a reference.

percentage of the total volume. The total porosity of the moulded samples ranged between 14.6 and 69.6 %. The lowest porosity is observed for the sample treated at room temperature (14.6 %). Porosity increased up to 400 °C because of organic compounds being removed from the AAM. An increase in pores size (2–10 μm) was observed as a consequence of the decomposition of organic binders present in the mineral wool (GW and SW) and organic material present in the BA. The results of TG-MS revealed that organic binders in GW and SW started to decompose into CO₂ at around 230 °C. The decomposition and removal of organic compounds from AAMs continued up to 550 °C (Fig. 5), meaning that the porosity of the material increased up to 550 °C. In BA, cellulose, which remained in the ash because of incomplete combustion, did not react with the alkali; organic materials present in the mineral wools partially reacted during the mixing of the slurry (which was

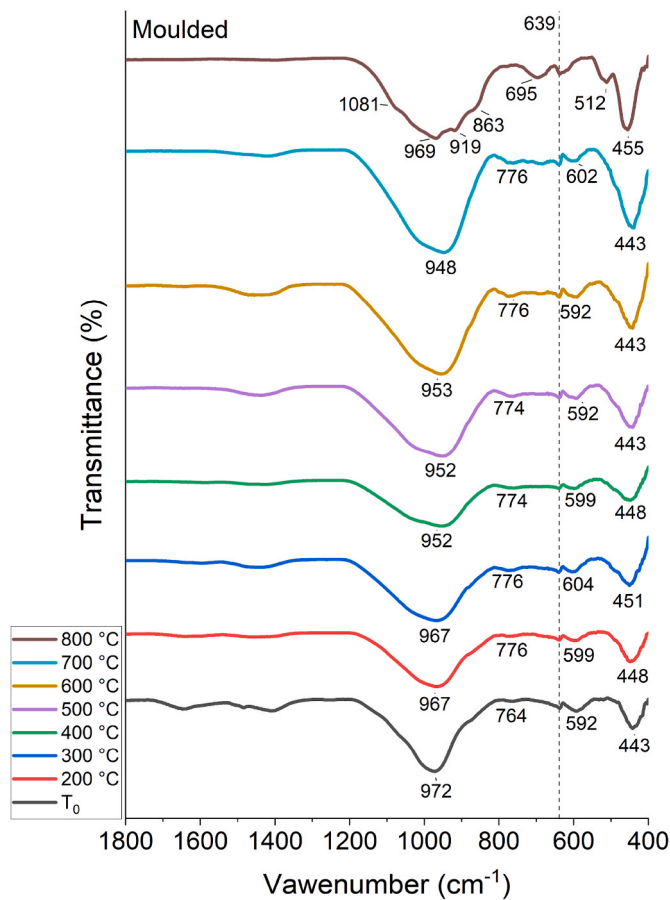


Fig. 13. FTIR spectra of the moulded samples at T_0 and at elevated temperatures (200, 300, 400, 500, 600, 700, and 800 °C).

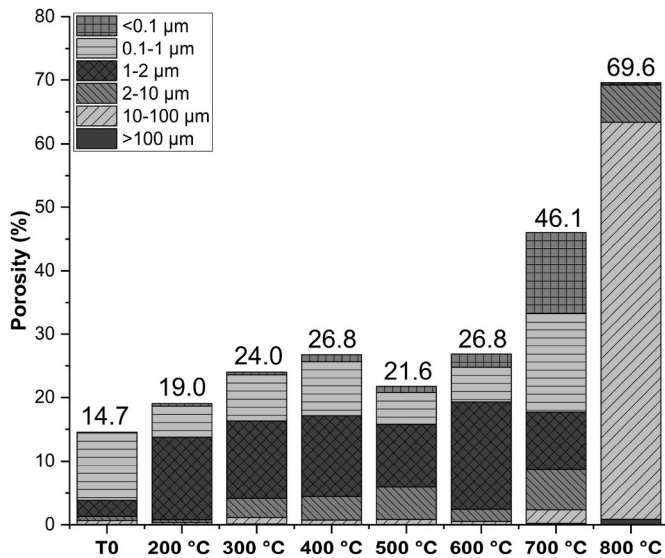


Fig. 14. Pore size distribution in the moulded samples treated at different elevated temperatures with T_0 as the reference temperature.

detected by the release of gases such as NH_3 [40], potentially various organic volatile compounds, and porosity of the AAM without the introduction of foaming agents). The increase in porosity at 200 °C was attributed to the dehydration and formation of cracks, and therefore, a decrease in mechanical strength. At 300 °C and especially at 400 °C, the

organic material from BA started to combust, giving the material a higher porosity and even lower mechanical strength. Given that porosity decreased at 500 °C and the skeletal density increased (Table 5), this is considered the sintering temperature. However, the mechanical strengths were still low (Fig. 10) because of the structural changes such as the formation of additional pores and cracks after dehydration, release of various gases and total combustion of cellulose. At 600 °C the porosity increased again because of the slight sample expansion that more significant at 700 °C. As expected from the inflated structure of the sample, the total porosity was the highest after treatment at 800 °C, and it reached a value of 69.6 % accompanied by a significant increase in the number of pores sized 10–100 μm . This is consistent with the mechanical properties (Fig. 10); changes in the inner crystalline structure indicated by the XRD (Fig. 12) and FTIR (Fig. 13) analyses; and the deformation of the amorphous gel as a consequence of the decomposition of $CaCO_3$, as shown in Fig. 5, which shows that peaks belonging to $CaCO_3$ significantly decreased after firing at 800 °C, in agreement with previous reports that the decomposition of $CaCO_3$ starts at 750 °C [88].

The geometrical density is calculated from the mass and outer dimensions of the samples (i.e. the volume) while the bulk density is the density calculated through MIP measurements, where the volume of the material is measured as the difference between the total penetrometer volume and the volume of mercury occupying open pores in the sample with a diameter less than approximately 1 mm. The skeletal density was calculated from the density measured by MIP, where the volume is the bulk volume minus the volume of pores filled by mercury. This density was close to the real density of the solid part of the material. All values are listed in Table 5.

3.3.6. SEM micrographs of the thermally treated samples

The thermally treated moulded AAMs are observed in the BSE mode; micrographs of the polished samples are presented in Fig. 15. SED-EDXS point analyses of the thermally treated samples are provided in the Supplementary Material (Text S3 and Table S3). The micrographs show the presence of unreacted mineral wool fibres that did not dissolve during alkali activation. The fibres were uniformly distributed and randomly oriented in the binder matrix, as observed in the fractured T_0 sample (Fig. 15). Some ‘shoots’ are observed as larger particles with a more rounded shape [89]. Unreacted particles from other precursors are also present. Microcracks present at T_0 indicate a loss of water during hardening because of pre-treating the sample. Although the samples cured at room temperature did not exhibit visible cracks, microcracks may occur as a result of shrinkage. The deformations in the samples occurred as a competition between thermal expansion (the reaction is self-enhanced by the temperature rise due to the heat release of the exothermic reaction caused by the dissolution of the precursors in the alkaline solution) and autogenous shrinkage [90]. Additional stress which can contribute to the crack formations can arise from thermal dilatation (during firing to and cooling down) when samples are exposed to the elevated temperature. The microstructures at T_0 and 200 °C are similar; however, at 200 °C, cracks are observed due to the dehydration process. More cracks appeared in the structure because the organic material decomposed with an increase in temperature, and this led to the movement of gases in and out of the structure. At 500 °C, the microstructure significantly changed in comparison to that at T_0 , 200, 300 and 400 °C (see the right-hand column in Fig. 15, which shows the non-polished sample). According to dilatometric studies (Fig. 9), the samples started to significantly expand at 630 °C, while the microstructure started to change at around 500 °C (based on SEM). However, the XRD analysis did not reveal any differences in the mineralogy of AAMs at this temperature (Fig. 12). At 600 °C, larger pores were observed and less unreacted mineral wool fibres were present. GW fibres, which have a melting point of approximately 700 °C [91] started to melt at approximately 500 °C, and this would have affected the structural changes (GW fibres can only be exposed to temperatures of 600 °C for a short period of time and longer periods of exposure to temperatures

Table 5Total porosity, skeletal, bulk, and geometrical densities for the moulded samples treated at different elevated temperatures and T_0 as the reference sample.

	T_0	200 °C	300 °C	400 °C	500 °C	600 °C	700 °C	800 °C
Total porosity (%)	14.7	19.0	24.0	26.8	21.6	26.8	46.1	69.6
Skeletal density (g cm^{-3})	2.33	2.39	2.51	2.44	2.59	2.45	2.23	2.41
Bulk density (g cm^{-3})	1.99	1.94	1.91	1.79	1.77	1.80	1.21	0.73
Geometrical density (g cm^{-3})	1.92	1.86	1.75	1.69	1.68	1.61	1.01	0.75

<500 °C before the fibre melts [45]). Because GW contains approximately 16 wt% Na_2O , it may act as a fluxing agent [91], decreasing the sintering temperature. Changes in the AAM network at 700 °C are shown in Fig. 15. FTIR and XRD (Figs. 12 and 13) did not confirm these changes; however, the MIP results (increased porosity, Fig. 14) and mechanical properties (decreased compressive and bending strengths, Fig. 10) confirmed these changes. These changes were viewed as the deterioration of the AAM network, whereas non-reacted parts of the precursors remained intact. However, at 800 °C, a completely different microstructure was observed, indicating a foamed (expanded) highly porous material, as proven by the MIP analysis (Fig. 14). In addition to the complete change in the AAM network, the non-reacted parts of the precursors were no longer observed.

3.3.7. X-ray computed microtomography of the thermally treated samples

An increase in temperature thermally degrades the samples, and this is non-destructively monitored using X-ray computed microtomography. Three microstructural properties were determined on the thermally treated samples (density, porosity, and shrinkage/expansion); first on the sample cured at room temperature (T_0), and then, on the thermally treated samples (200, 500, and 800 °C).

The microstructural evolution of the moulded samples is investigated at elevated temperatures as shown in Fig. 16. The microtomography results showed that the moulded sample prepared at room temperature (T_0) included internal cracks, which widened at elevated temperatures (200, 500, and 800 °C), leading to significant cracking, spallation, and the formation of additional pores at 800 °C. This was confirmed by the MIP and SEM analyses, with the porosity significantly increasing at 800 °C (as shown in Figs. 14 and 15). A crack formed in the middle of the moulded sample (T_0) with a length of approximately 31 mm in the YZ cross-section. The 3D volume of the large crack is shown in Fig. 16 (marked in blue) alongside the largest air voids. The volume of the cracks increased because of elevated temperatures. The volume of air expands when it is heated, causing tensile stress within the structure, which forms cracks because of excessive fracture toughness [92].

The size distribution of air voids is extremely uneven, and there are several unconnected air voids. One representative air void is selected to demonstrate changes in the volume of air voids at elevated temperatures, as shown in Fig. 17. The equivalent diameter (i.e. 2D is the diameter of the disk of the same area) and 3D volume (corresponding to the number of voxels of the object multiplied by the volume of a single voxel) of such a void were determined at a specific sample location at different temperatures; the total volume of the selected region of interest (ROI) was a $4 \times 4 \times 4 \text{ mm}^3$ block extracted from the whole sample. Cross-sectional analysis of the ROI showed that the selected air void (Fig. 17) was relatively well rounded with no sharp corners at the edges; this indicated that the prepared paste was loose. The diameter (and 3D volume) of the void was 1.65 mm (2.54 mm^3) at ambient temperature, 1.62 mm (2.23 mm^3) at 200 °C, and 1.59 mm (2.08 mm^3) at 500 °C. Very small differences occurred up to 500 °C, indicating a small amount of shrinkage; however, at 800 °C, the pores were connected to the crack because of expansion (Fig. 17).

The microstructural fracture phenomena in the 3D-printed samples were visually compared with those of the moulded samples using microtomography. The results showed surface damage to the 3D-printed samples, which was barely visible even at the highest temperature (800 °C), and internal damage with cracking. This demonstrates the

effect of interconnected porosity on interfacial cracking and prevents the crack from extending into the surrounding solids (Fig. 17).

The porosity of 3D-printed samples showed changes in the inner structure from the time of exposure to elevated temperatures (Fig. 18). Fig. 18 represent 2D grayscale images and 3D images of the inner structure with segmented pore space in colour (determined by Material Statistics module before Labelling module). In addition to the pore size diameter, porosity of presented pores increases because of elevated temperatures, from 1.1 % in the T_0 sample to 1.3 %, 3.7 %, and 16.5 % following exposure to 200, 500, and 800 °C, respectively.

The porosity of the moulded samples was determined immediately after exposure to elevated temperatures. Fig. 19 shows the changes in porosity; both porosity and pore size diameter increase because of the elevated temperatures. The porosity increased from 1.2 % at T_0 to 1.5 %, 4.8 %, and 30 % at 200, 500 and 800 °C, respectively. Pore size distribution analysis was conducted after determining the change in porosity, and the number and size of pores in both the T_0 sample and those exposed to 200, 500 and 800 °C were identified. A pore-size distribution analysis was performed, as shown in Fig. 19. The same trend was observed in both the moulded and 3D-printed samples, with the T_0 sample showing a lower number of pores sized between 56 and 200 μm in the diameter; the number of pores (as well as their diameter) increased when the samples were thermally treated at 200, 500, and 800 °C. Some pores were connected in one direction and sometimes aligned with cracks and fractures, especially in the sample exposed to the highest temperature. Pore size distribution analysis showed that pores in the sample exposed to 800 °C were considerably larger than those in the other samples, with a diameter of over 0.2 mm. Further, different pore shapes and a unique internal pore structure were also presented. Fig. 19 shows that the T_0 sample and the sample treated at 200 °C has fewer pores between 56 and 200 μm in diameter, whereas an increase in the number of pores is observed in the samples thermally treated at 500 and 800 °C (Fig. 19).

Any shrinkage/expansion in the volume of the moulded samples was determined from the 3D data of the scanned images obtained using X-ray computed microtomography. The total sample volume obtained after interactive thresholding was also considered. The average change in volume after exposure to elevated temperatures was -4.2% at 200 °C and -9.4% at 500 °C, indicating slight shrinkage. However, at 800 °C, an expansion of 91.5 % was observed, which was also in general agreement with the dilatometric results. Shrinkage/expansion in the dimensions and volume of the 3D-printed samples at elevated temperatures were similar to those of the moulded samples; however, the values were slightly lower. Slight shrinkage was seen at the lower temperatures, with values of -4.1% and -8.8% at 200 °C and 500 °C, respectively, while an expansion of 74.3 % was observed at 800 °C, which is about 20 % less than that observed in the moulded samples. Thus, pores in the printed samples exhibit a significant gas-acceptance volume to avoid a decrease in mechanical strength resulting from the decomposition of parts of the material at elevated temperatures.

4. Conclusions

This study has revealed significant insights into the potential of an AAM based on waste mineral wool for 3D printing applications. The suitability of this AAM was demonstrated through the successful production of 3D-printed samples. The key findings and conclusions are as

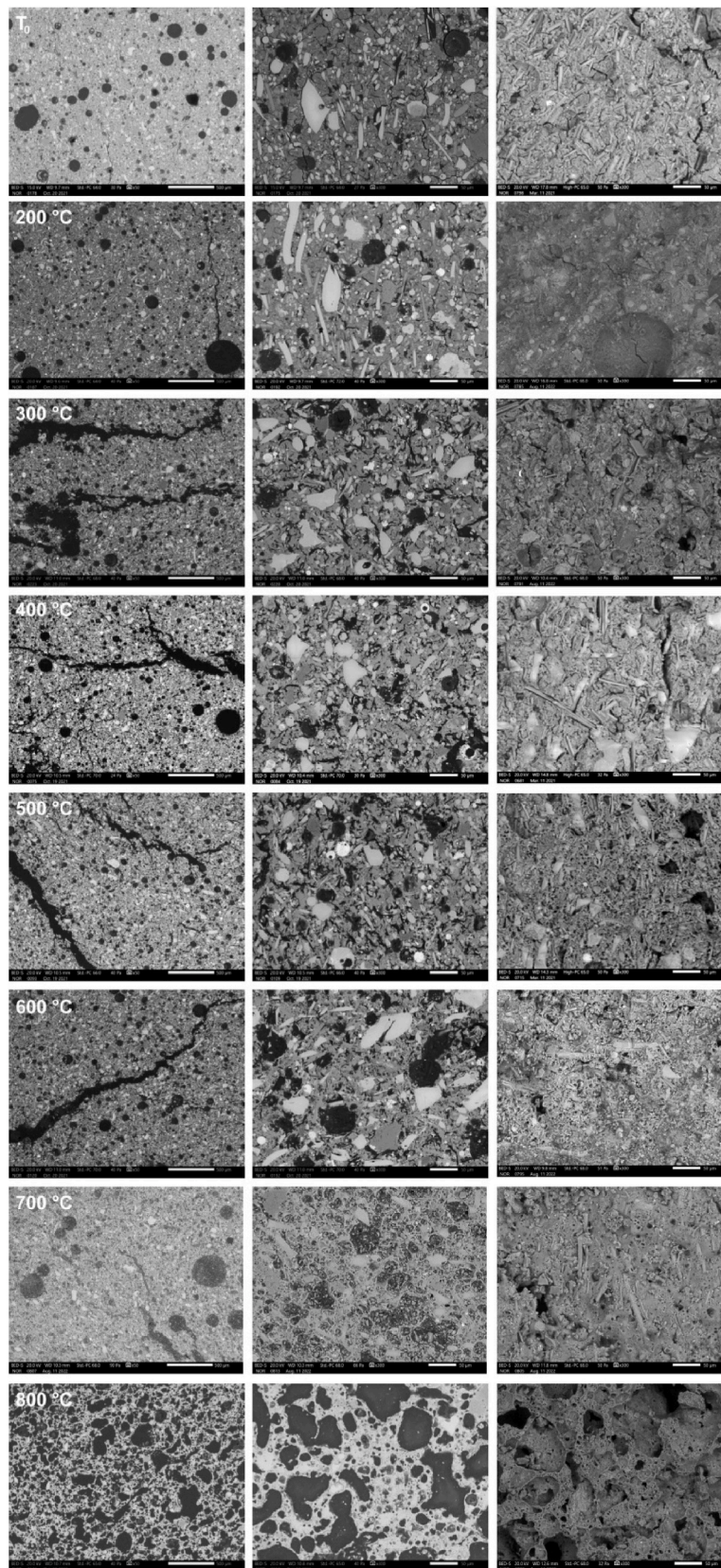


Fig. 15. SEM micrographs of the samples at T_0 and after thermal treatment at 200, 300, 400, 500, 600, 700, and 800 °C. The SEM microstructures are 50-times magnified on the left and 300-times in the middle and on the right-hand side. The samples in the middle and on the left represent a polished sample, whereas those on the right are fracture samples.

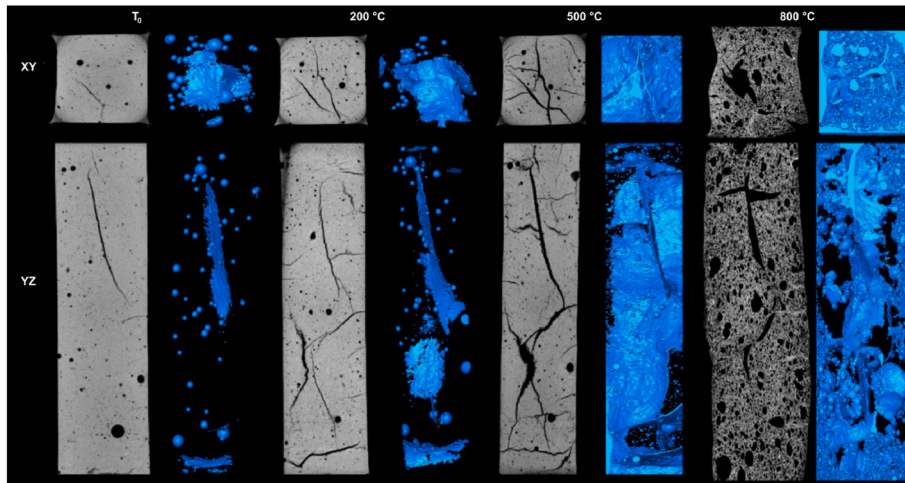


Fig. 16. Grayscale images in the XY and YZ directions and the 3D images showing the volume of pores and cracks in the moulded samples exposed to elevated temperatures.

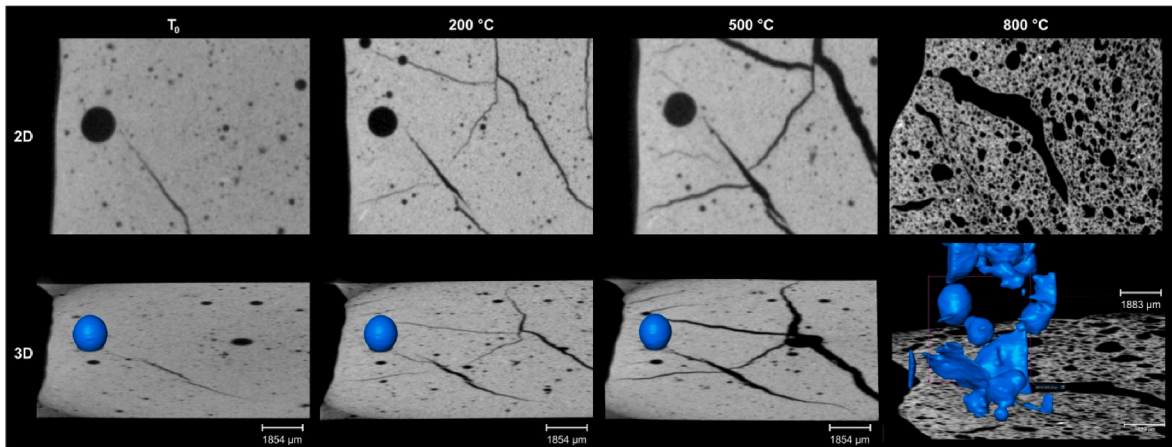


Fig. 17. Small changes in the representative air void caused by elevated temperatures shown as (a) a cross section in the XY direction and (b) 3D volume.

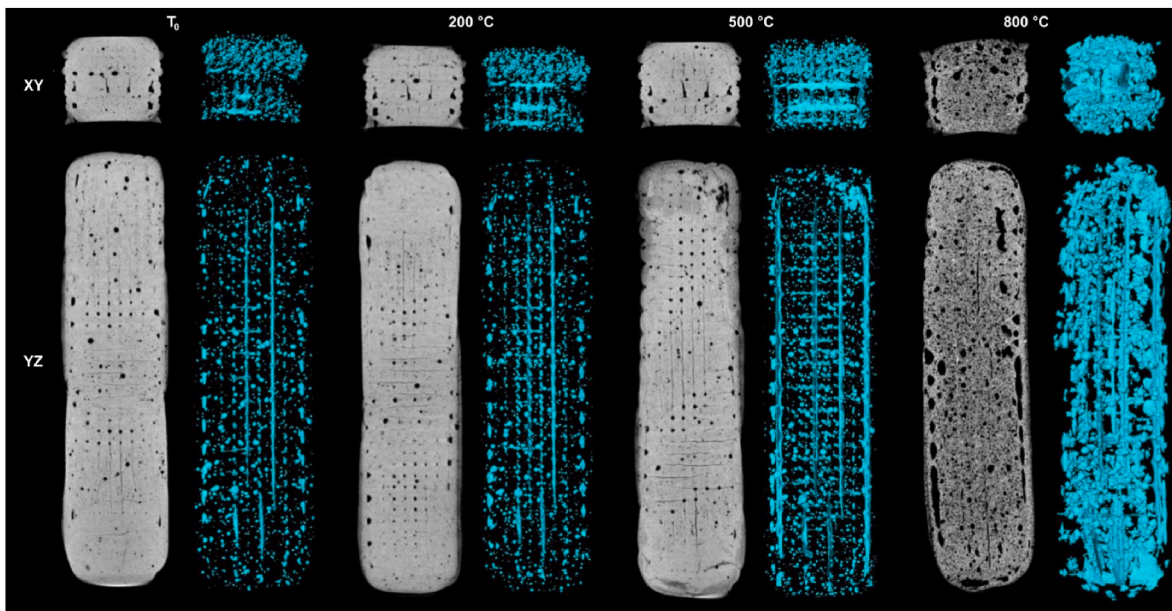


Fig. 18. 2D grayscale images in the XY and YZ directions and the 3D coloured images of the pore volumes (segmented pore space shown in three-dimensions) in the 3D-printed samples exposed to elevated temperatures, as determined by X-ray computed microtomography.

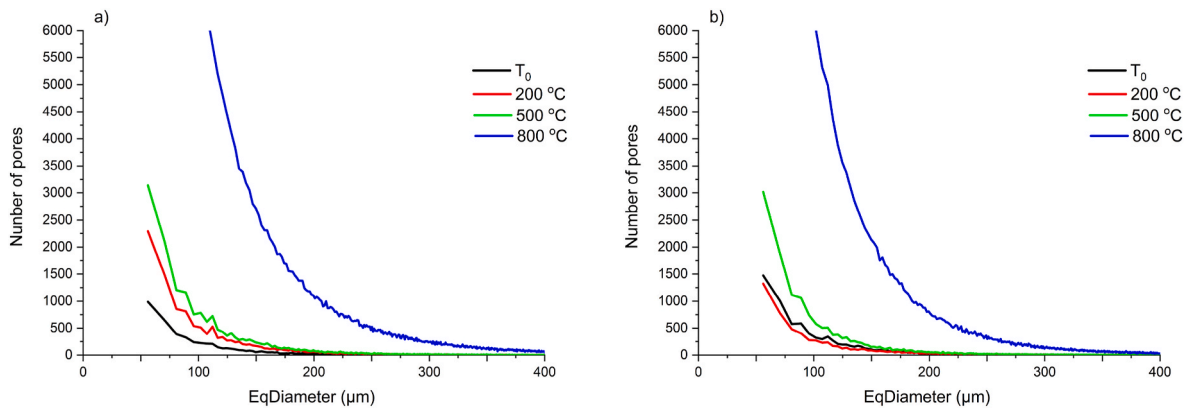


Fig. 19. Pore size distribution for (a) the moulded and (b) 3D-printed samples, as determined by X-ray computed microtomography and presented as the number of pores with respect to pore size.

follows:

- The selection of the mixture for 3D printing based on workability, viscosity, extrusion, and buildability. By incorporating mineral wool (SW and GW), along with co-binders such as CAC, Mic, and BA, the AAM was optimised. The addition of CAC proved accelerating of material hardening. Despite the challenge posed by increased viscosity upon the addition of BA, this trade-off was mitigated by improved buildability. Ultimately, the most suitable mixture for 3D printing was achieved with the incorporation of Mic.
- Through the addition of mineral wool and co-binders, the alkali-activated 3D-printed products exhibited compressive strengths exceeding 50 MPa after 28 days of curing at T_0 .
- The exposed moulded and 3D-printed samples to elevated temperatures up to 800 °C showcased their chemical and mineralogical stability up to 700 °C. However, at 800 °C, new mineralogical phases emerged, leading to a decrease in the amorphous content from approximately 86 wt% to 46 wt%.
- Dilatometric analysis highlighted the stability of samples up to around 600 °C. Microtomography, revealing insights into the microstructure, indicated shrinkage at 500 °C and significant expansion at 800 °C. Notably, 3D-printed samples demonstrated less shrinkage and a lower degree of expansion compared to moulded samples due to the distinctive artificial porosity imparted by the printing process.
- The study highlights the central role of porosity in determining mechanical strength, regardless of preparation method. While increased porosity can contribute to lower mechanical strength, it also serves as a channel for the release of gasses and gives 3D-printed samples an advantage over their moulded counterparts.

In summary, this investigation offers a novel perspective on the utilization of waste mineral wool and co-binders in the development of alkali-activated mixtures for 3D printing. The findings underscore the robust mechanical performance and thermal stability of these materials, positioning them as promising candidates for applications requiring endurance under elevated temperatures. The study not only contributes to the field of construction materials but also indicates the potential way for sustainable recycling practices.

Declaration of competing interest

The authors declare that they have no known competing financial interests or personal relationships that could have appeared to influence the work reported in this paper.

Data availability

Data will be made available on request.

Acknowledgement

This project received funding from the European Union's Framework Program for Research and Innovation Horizon 2020 under Grant Agreement number 821000. The Metrology Institute of the Republic of Slovenia is acknowledged for its use of XRF. The financial support received from the Slovenian Research Agency for programmes P2-0273.

Appendix A. Supplementary data

Supplementary data to this article can be found online at <https://doi.org/10.1016/j.cemconcomp.2024.105445>.

References

- [1] E. Commission, Clean Energy for All Europeans Package, 2019. https://ec.europa.eu/energy/topics/energy-strategy/clean-energy-all-europeans_en.
- [2] E. Commission, Construction and Demolition Waste, 2020. https://ec.europa.eu/environment/topics/waste-and-recycling/construction-and-demolition-waste_en.
- [3] J. Malda, J. Visser, F.P. Melchels, T. Jüngst, W.E. Hennink, W.J.A. Dhert, J. Groll, D.W. Hutmacher, 25th anniversary article: engineering hydrogels for biofabrication, *Adv. Mater.* 25 (2013) 5011–5028, <https://doi.org/10.1002/adma.201302042>.
- [4] S.V. Murphy, A. Atala, 3D bioprinting of tissues and organs, *Nat. Biotechnol.* 32 (2014) 773–785, <https://doi.org/10.1038/nbt.2958>.
- [5] A. Kashani, T.D. Ngo, Optimisation of mixture properties for 3D printing of geopolymer concrete, in: *ISARC. Proc. Int. Symp. Autom. Robot. Constr., IAARC Publications*, 2018, pp. 1–8.
- [6] S. Pessoa, A.S. Guimarães, S.S. Lucas, N. Simões, 3D printing in the construction industry—A systematic review of the thermal performance in buildings, *Renew. Sustain. Energy Rev.* 141 (2021) 110794.
- [7] A. Kazemian, X. Yuan, E. Cochran, B. Khoshnevis, Cementitious materials for construction-scale 3D printing: laboratory testing of fresh printing mixture, *Construct. Build. Mater.* 145 (2017) 639–647, <https://doi.org/10.1016/j.conbuildmat.2017.04.015>.
- [8] C. Gosselin, R. Duballet, P. Roux, N. Gaudillière, J. Dirrenberger, P. Morel, Large-scale 3D printing of ultra-high performance concrete – a new processing route for architects and builders, *Mater. Des.* 100 (2016) 102–109, <https://doi.org/10.1016/j.matdes.2016.03.097>.
- [9] H. Jeong, S.-J. Han, S.-H. Choi, Y.-J. Lee, S.T. Yi, K.S. Kim, Rheological property criteria for buildable 3D printing concrete, *Materials* 12 (2019) 657.
- [10] H. Alghamdi, S.A.O. Nair, N. Neithalath, Insights into material design, extrusion rheology, and properties of 3D-printable alkali-activated fly ash-based binders, *Mater. Des.* 167 (2019) 107634.
- [11] H. Zhong, M. Zhang, 3D printing geopolymers: a review, *Cem. Concr. Compos.* (2022) 104455.
- [12] Y. Zhang, Y. Zhang, G. Liu, Y. Yang, M. Wu, B. Pang, Fresh properties of a novel 3D printing concrete ink, *Construct. Build. Mater.* 174 (2018) 263–271, <https://doi.org/10.1016/j.conbuildmat.2018.04.115>.
- [13] S.A.O. Nair, H. Alghamdi, A. Arora, I. Mehdipour, G. Sant, N. Neithalath, Linking fresh paste microstructure, rheology and extrusion characteristics of cementitious

- binders for 3D printing, *J. Am. Ceram. Soc.* 102 (2019) 3951–3964, <https://doi.org/10.1111/jace.16305>.
- [14] N. Roussel, Rheological requirements for printable concretes, *Cement Concr. Res.* 112 (2018) 76–85, <https://doi.org/10.1016/j.cemconres.2018.04.005>.
- [15] F. Bos, R. Wolfs, Z. Ahmed, T. Salet, Additive manufacturing of concrete in construction: potentials and challenges of 3D concrete printing, *Virtual Phys. Prototyp.* 11 (2016) 209–225.
- [16] S.C. Paul, Y.W.D. Tay, B. Panda, M.J. Tan, Fresh and hardened properties of 3D printable cementitious materials for building and construction, *Arch. Civ. Mech. Eng.* 18 (2018) 311–319, <https://doi.org/10.1016/j.acme.2017.02.008>.
- [17] N. Roussel, Correlation between yield stress and slump: comparison between numerical simulations and concrete rheometers results, *Mater. Struct.* 39 (2006) 501, <https://doi.org/10.1617/s11527-005-9035-2>.
- [18] M. Papachristoforou, V. Mitsopoulos, M. Stefanidou, Evaluation of workability parameters in 3D printing concrete, *Procedia Struct. Integr.* 10 (2018) 155–162, <https://doi.org/10.1016/j.prostr.2018.09.023>.
- [19] T.T. Le, S.A. Austin, S. Lim, R.A. Buswell, A.G.F. Gibb, T. Thorpe, Mix design and fresh properties for high-performance printing concrete, *Mater. Struct.* 45 (2012) 1221–1232.
- [20] J.J. Biernacki, J.W. Bullard, G. Sant, K. Brown, F.P. Glasser, S. Jones, T. Ley, R. Livingston, L. Nicoleau, J. Olek, Cements in the 21st century: challenges, perspectives, and opportunities, *J. Am. Ceram. Soc.* 100 (2017) 2746–2773.
- [21] M. Hambach, D. Volkmer, Properties of 3D-printed fiber-reinforced Portland cement paste, *Cem. Concr. Compos.* 79 (2017) 62–70, <https://doi.org/10.1016/j.cemconcomp.2017.02.001>.
- [22] B. Nematollahi, P. Vijay, J. Sanjayan, A. Nazari, M. Xia, V. Naidu Nerella, V. Mechtcherine, Effect of polypropylene fibre addition on properties of geopolymers made by 3D printing for digital construction, *Materials* 11 (2018) 2352.
- [23] S. Christ, M. Schnabel, E. Vorndran, J. Groll, U. Gbureck, Fiber reinforcement during 3D printing, *Mater. Lett.* 139 (2015) 165–168.
- [24] T.T. Le, S.A. Austin, S. Lim, R.A. Buswell, R. Law, A.G.F. Gibb, T. Thorpe, Hardened properties of high-performance printing concrete, *Cement Concr. Res.* 42 (2012) 558–566.
- [25] T. Wangler, E. Lloret, L. Reiter, N. Hack, F. Gramazio, M. Kohler, M. Bernhard, B. Dillenburger, J. Buchli, N. Roussel, Digital concrete: opportunities and challenges, *RILEM Tech. Lett.* 1 (2016) 67–75.
- [26] M. Hojati, S. Nazarian, J.P. Duarte, N. Ashrafi, F. Craveiro, S. Bilén, 3D Printing of Concrete: A Continuous Exploration of Mix Design and Printing Process, 2018.
- [27] M. Chougan, S.H. Ghaffar, P. Sikora, S.-Y. Chung, T. Rucinska, D. Stephan, A. Albar, M.R. Swash, Investigation of additive incorporation on rheological, microstructural and mechanical properties of 3D printable alkali-activated materials, *Mater. Des.* 202 (2021) 109574.
- [28] M. Xia, J. Sanjayan, Method of formulating geopolymer for 3D printing for construction applications, *Mater. Des.* 110 (2016) 382–390, <https://doi.org/10.1016/j.matdes.2016.07.136>.
- [29] B. Panda, S.C. Paul, L.J. Hui, Y.W.D. Tay, M.J. Tan, Additive manufacturing of geopolymer for sustainable built environment, *J. Clean. Prod.* 167 (2017) 281–288, <https://doi.org/10.1016/j.jclepro.2017.08.165>.
- [30] B. Panda, C. Unluer, M.J. Tan, Investigation of the rheology and strength of geopolymer mixtures for extrusion-based 3D printing, *Cem. Concr. Compos.* 94 (2018) 307–314, <https://doi.org/10.1016/j.cemconcomp.2018.10.002>.
- [31] B. Panda, M.J. Tan, Experimental study on mix proportion and fresh properties of fly ash based geopolymer for 3D concrete printing, *Ceram. Int.* 44 (2018) 10258–10265, <https://doi.org/10.1016/j.ceramint.2018.03.031>.
- [31] S.H. Bong, M. Xia, B. Nematollahi, C. Shi, Ambient temperature cured 'just-add-water' geopolymer for 3D concrete printing applications, *Cem. Concr. Compos.* 121 (2021) 104060.
- [33] A. Bagheri, C. Cremona, Formulation of mix design for 3D printing of geopolymers: a machine learning approach, *Mater. Adv.* 1 (2020) 720–727, <https://doi.org/10.1039/D0MA00036A>.
- [34] A.U. Rehman, V.M. Sglavo, 3D printing of geopolymer-based concrete for building applications, *Rapid Prototyp. J.* 26 (2020) 1783–1788.
- [35] M. Chougan, S. Hamidreza Ghaffar, M. Jahanzat, A. Albar, N. Mujaddedi, R. Swash, The influence of nano-additives in strengthening mechanical performance of 3D printed multi-binder geopolymer composites, *Construct. Build. Mater.* 250 (2020) 118928, <https://doi.org/10.1016/j.conbuildmat.2020.118928>.
- [36] P. Duxson, J.L. Provis, G.C. Lukey, S.W. Mallicoat, W.M. Kriven, J.S.J. van Deventer, Understanding the relationship between geopolymer composition, microstructure and mechanical properties, *Colloids Surfaces A Physicochem. Eng. Asp.* 269 (2005) 47–58, <https://doi.org/10.1016/J.COLSURFA.2005.06.060>.
- [37] A. Kashani, J.L. Provis, G.G. Qiao, J.S.J. van Deventer, The interrelationship between surface chemistry and rheology in alkali activated slag paste, *Construct. Build. Mater.* 65 (2014) 583–591, <https://doi.org/10.1016/j.conbuildmat.2014.04.127>.
- [38] O. Väntsi, T. Kärki, Mineral wool waste in Europe: a review of mineral wool waste quantity, quality, and current recycling methods, *J. Mater. Cycles Waste Manag.* 16 (2014) 62–72, <https://doi.org/10.1007/s10163-013-0170-5>.
- [39] European Parliament, 2008/98/EC: Directive of the European Parliament and of the Council of 19 November 2008 on Waste and Repealing Certain Directives, vol. 2008, 2008. <https://ec.europa.eu/environment/waste/framework/>.
- [40] J. Yliniemi, R. Ramaswamy, T. Luukkonen, O. Laitinen, Á.N. de Sousa, M. Huuhtanen, M. Illikainen, Characterization of mineral wool waste chemical composition, organic resin content and fiber dimensions: aspects for valorization, *Waste Manag.* 131 (2021) 323–330, <https://doi.org/10.1016/j.wasman.2021.06.022>.
- [41] M. Pavlin, B. Horvat, A. Frankovič, V. Ducman, Mechanical, microstructural and mineralogical evaluation of alkali-activated waste glass and stone wool, *Ceram. Int.* (2021), <https://doi.org/10.1016/j.ceramint.2021.02.068>.
- [42] J. Yliniemi, P. Kinnunen, P. Karinkanta, M. Illikainen, Utilization of mineral wools as alkali-activated material precursor, *Materials* 9 (2016) 312, <https://doi.org/10.3390/ma9050312>.
- [43] J. Yliniemi, B. Walkley, J.L. Provis, P. Kinnunen, M. Illikainen, Nanostructural evolution of alkali-activated mineral wools, *Cem. Concr. Compos.* 106 (2020) 103472, <https://doi.org/10.1016/J.CEMCONCOMP.2019.103472>.
- [44] R.J. Flatt, P. Bowen, Yodel: a yield stress model for suspensions, *J. Am. Ceram. Soc.* 89 (2006) 1244–1256, <https://doi.org/10.1111/j.1551-2916.2005.00888.x>.
- [45] S. Kowatsch, in: L. Pilato (Ed.), *Mineral Wool Insulation Binders BT - Phenolic Resins: A Century of Progress*, Springer Berlin Heidelberg, Berlin, Heidelberg, 2010, pp. 209–242, https://doi.org/10.1007/978-3-642-04714-5_10.
- [46] J. Yliniemi, B. Walkley, J.L. Provis, P. Kinnunen, M. Illikainen, Influence of activator type on reaction kinetics, setting time, and compressive strength of alkali-activated mineral wools, *J. Therm. Anal. Calorim.* (2020), <https://doi.org/10.1007/s10973-020-09651-6>.
- [47] M. Pavlin, B. Horvat, M. Češnovar, V. Ducman, The preparation and characterization of low-temperature foams based on the alkali activation of waste stone wool, *Ceram. Int.* 48 (2022) 17668–17681, <https://doi.org/10.1016/j.ceramint.2022.03.037>.
- [48] P.N. Lemougna, A. Adediran, J. Yliniemi, T. Luukkonen, M. Illikainen, Effect of organic resin in glass wool waste and curing temperature on the synthesis and properties of alkali-activated pastes, *Mater. Des.* 212 (2021) 110287, <https://doi.org/10.1016/j.matdes.2021.110287>.
- [49] K. König, K. Traven, M. Pavlin, V. Ducman, Evaluation of locally available amorphous waste materials as a source for alternative alkali activators, *Ceram. Int.* (2020), <https://doi.org/10.1016/j.ceramint.2020.10.059>.
- [50] J. Yliniemi, T. Luukkonen, A. Kaiser, M. Illikainen, Mineral Wool Waste-Based Geopolymers, 2019, <https://doi.org/10.1088/1755-1315/297/1/012006>.
- [51] J. Yliniemi, B. Walkley, J.L. Provis, P. Kinnunen, M. Illikainen, Influence of activator type on reaction kinetics, setting time, and compressive strength of alkali-activated mineral wools, *J. Therm. Anal. Calorim.* 144 (2021) 1129–1138.
- [52] M. Pavlin, B. Horvat, V. Ducman, Pilot production of façade panels: variability of mix design, in: 5th Int. Conf. Technol. Bus. Model. Circ. Econ., 2023, p. 25.
- [53] C. Zhang, V.N. Nerella, A. Krishna, S. Wang, Y. Zhang, V. Mechtcherine, N. Banthia, Mix design concepts for 3D printable concrete: a review, *Cem. Concr. Compos.* 122 (2021) 104155.
- [54] H. Rietveld, A profile refinement method for nuclear and magnetic structures, *J. Appl. Crystallogr.* 2 (1969) 65–71, <https://doi.org/10.1107/S0021889869006558>.
- [55] Y. Chen, L. Jia, C. Liu, Z. Zhang, L. Ma, C. Chen, N. Banthia, Y. Zhang, Mechanical anisotropy evolution of 3D-printed alkali-activated materials with different GGBFS/FA combinations, *J. Build. Eng.* 50 (2022) 104126.
- [56] M. Pavlin, B. Horvat, V. Ducman, Preparation of façade panels based on alkali-activated waste mineral wool, their characterization and durability aspects, *Int. J. Appl. Ceram. Technol.* n/a (2022), <https://doi.org/10.1111/ijac.13998>.
- [57] P. Bosscher, R.L. Williams, L.S. Bryson, D. Castro-Lacouture, Cable-suspended robotic contour crafting system, *Autom. Construct.* 17 (2007) 45–55, <https://doi.org/10.1016/j.autcon.2007.02.011>.
- [58] B. Panda, C. Unluer, M.J. Tan, Extrusion and rheology characterization of geopolymer nanocomposites used in 3D printing, *Composites, Part B* 176 (2019) 107290.
- [59] B. Panda, S.C. Paul, N.A.N. Mohamed, Y.W.D. Tay, M.J. Tan, Measurement of tensile bond strength of 3D printed geopolymer mortar, *Measurement* 113 (2018) 108–116, <https://doi.org/10.1016/j.measurement.2017.08.051>.
- [60] S. Al-Qutaifi, A. Nazari, A. Bagheri, Mechanical properties of layered geopolymer structures applicable in concrete 3D-printing, *Construct. Build. Mater.* 176 (2018) 690–699.
- [61] M. Rowles, B. O'connor, Chemical optimisation of the compressive strength of aluminosilicate geopolymers synthesised by sodium silicate activation of metakaolinite, *J. Mater. Chem.* 13 (2003) 1161–1165.
- [62] S. Rocca, A. van Zomeren, G. Costa, J.J. Dijkstra, R.N.J. Comans, F. Lombardi, Mechanisms contributing to the thermal analysis of waste incineration bottom ash and quantification of different carbon species, *Waste Manag.* 33 (2013) 373–381, <https://doi.org/10.1016/j.wasman.2012.11.004>.
- [63] V. Kumar, V.K. Singh, A. Srivastava, G.N. Agrawal, Low temperature synthesis of high alumina cements by gel-trapped Co-precipitation process and their implementation as castables, *J. Am. Ceram. Soc.* 95 (2012) 3769–3775.
- [64] P. Ludvig, J.M. Calixto, L.O. Ladeira, I.C.P. Gaspar, Using converter dust to produce low cost cementitious composites by in situ carbon nanotube and nanofiber synthesis, *Materials* 4 (2011) 575–584, <https://doi.org/10.3390/ma4030575>.
- [65] A.S. Khan, H. Khalid, Z. Sarfraz, M. Khan, J. Iqbal, N. Muhammad, M.A. Fareed, I. U. Rehman, Vibrational spectroscopy of selective dental restorative materials, *Appl. Spectrosc. Rev.* 52 (2017) 507–540, <https://doi.org/10.1080/05704928.2016.1244069>.
- [66] L. Fernández Carrasco, A. Fernández-Giménez, A. Palomo, Alkali activation of "Pozzolan-calcium aluminate cement" mixtures, in: 12th, *Int. Congr. Clin. Chem.* (2007).
- [67] Z. Zhang, H. Wang, J.L. Provis, Quantitative study of the reactivity of fly ash in geopolymerization by FTIR, *J. Sustain. Cem. Mater.* 1 (2012) 154–166.
- [68] M. Criado, A. Fernández-Jiménez, A. Palomo, Alkali activation of fly ash: effect of the SiO₂/Na₂O ratio: Part I: FTIR study, *Microporous Mesoporous Mater.* 106 (2007) 180–191.

- [69] F.B. Reig, J.V.G. Adelantado, M.C.M. Moya Moreno, FTIR quantitative analysis of calcium carbonate (calcite) and silica (quartz) mixtures using the constant ratio method. Application to geological samples, *Talanta* 58 (2002) 811–821, [https://doi.org/10.1016/S0039-9140\(02\)00372-7](https://doi.org/10.1016/S0039-9140(02)00372-7).
- [70] N.S. Salas, F.O. Gutiérrez, L.D.M. Murillo, Y.C. Ureña, S. Johnson, J.V. Baudrit, R. J. González-Paz, Synthesis and reinforcement of thermostable polymers using renewable resources, *J. Renew. Mater.* 5 (2017) 313–322.
- [71] V.F.F. Barbosa, K.J.D. MacKenzie, C. Thaumaturgo, Synthesis and characterisation of materials based on inorganic polymers of alumina and silica: sodium polysilicate polymers, *Int. J. Inorg. Mater.* 2 (2000) 309–317, [https://doi.org/10.1016/S1466-6049\(00\)00041-6](https://doi.org/10.1016/S1466-6049(00)00041-6).
- [72] M. Torres-Carrasco, A. Palomo, F. Puertas, *Sodium Silicate Solutions from Dissolution of Glass Wastes*, Statistical analysis, 2014.
- [73] B. Walkley, R. San Nicolas, M.-A. Sani, J.D. Gehman, J.S.J. van Deventer, J. L. Provis, Phase evolution of Na₂O–Al₂O₃–SiO₂–H₂O gels in synthetic aluminosilicate binders, *Dalton Trans.* 45 (2016) 5521–5535, <https://doi.org/10.1039/C5DT04878H>.
- [74] B.H.W.S. de Jong, G.E. Brown, Polymerization of silicate and aluminate tetrahedra in glasses, melts and aqueous solutions—II. The network modifying effects of Mg²⁺, K⁺, Na⁺, Li⁺, H⁺, OH⁻, F⁻, Cl⁻, H₂O, CO₂ and H₃O⁺ on silicate polymers, *Geochem. Cosmochim. Acta* 44 (1980) 1627–1642, [https://doi.org/10.1016/0016-7037\(80\)90216-1](https://doi.org/10.1016/0016-7037(80)90216-1).
- [75] Y. Xiao, A.C. Lasaga, Ab initio quantum mechanical studies of the kinetics and mechanisms of silicate dissolution: H⁺(H₃O⁺) catalysis, *Geochem. Cosmochim. Acta* 58 (1994) 5379–5400, [https://doi.org/10.1016/0016-7037\(94\)90237-2](https://doi.org/10.1016/0016-7037(94)90237-2).
- [76] A. Fernández-Jiménez, A. Palomo, Mid-infrared spectroscopic studies of alkali-activated fly ash structure, *Microporous Mesoporous Mater.* 86 (2005) 207–214, <https://doi.org/10.1016/j.micromeso.2005.05.057>.
- [77] A. Fernández-Jiménez, F. Puertas, I. Sobrados, J. Sanz, Structure of calcium silicate hydrates formed in alkaline-activated slag: influence of the type of alkaline activator, *J. Am. Ceram. Soc.* 86 (2003) 1389–1394, <https://doi.org/10.1111/j.1151-2916.2003.tb03481.x>.
- [78] Y. Ming-qing, Experiment of degassing efficiency for different viscosity drilling fluids, *Xinjing Pet. Geol.* 32 (2011) 675.
- [79] S. Diener, G. Franchin, N. Achilles, T. Kuhnt, F. Rösler, N. Katsikis, P. Colombo, X-ray microtomography investigations on the residual pore structure in silicon nitride bars manufactured by direct ink writing using different printing patterns, *Open Ceram* 5 (2021) 100042.
- [80] M. Moini, J. Olek, B. Magee, P. Zavattieri, J. Youngblood, Additive manufacturing and characterization of architected cement-based materials via X-ray micro-computed tomography, in: *RILEM Int. Conf. Concr. Digit. Fabr.*, Springer, 2018, pp. 176–189.
- [81] R. Moini, A. Baghaie, F.B. Rodriguez, P.D. Zavattieri, J.P. Youngblood, J. Olek, Quantitative microstructural investigation of 3D-printed and cast cement pastes using micro-computed tomography and image analysis, *Cement Concr. Res.* 147 (2021) 106493.
- [82] L. Vickers, A. Van Riessen, W.D.A. Rickard, *Fire-resistant Geopolymers: Role of Fibres and Fillers to Enhance Thermal Properties*, Springer, 2015.
- [83] V. Ducman, Foaming process of waste glass using CaCO₃, MnO₂ and water-glass as foaming agents, in: *Sustain. Waste Manag. Recycl. Proc. Int. Conf. Organ. By Concr. Mason. Res. Kingst. Univ. London*, Thomas Telford Publ., London, UK, 2004, pp. 59–66.
- [84] W.D.A. Rickard, G.J.G. Gluth, K. Pistol, In-situ thermo-mechanical testing of fly ash geopolymer concretes made with quartz and expanded clay aggregates, *Cement Concr. Res.* 80 (2016) 33–43, <https://doi.org/10.1016/j.cemconres.2015.11.006>.
- [85] S.A. Bernal, J.L. Provis, V. Rose, R. Mejía de Gutierrez, Evolution of binder structure in sodium silicate-activated slag-metakaolin blends, *Cem. Concr. Compos.* 33 (2011) 46–54, <https://doi.org/10.1016/j.cemconcomp.2010.09.004>.
- [86] C.A. Rees, J.L. Provis, G.C. Lukey, J.S.J. van Deventer, In situ ATR-FTIR study of the early stages of fly ash geopolymer gel formation, *Langmuir* 23 (2007) 9076–9082, <https://doi.org/10.1021/la701185g>.
- [87] E. Prud'homme, P. Michaud, E. Joussein, J.-M. Clacens, S. Arii-Clacens, I. Sobrados, C. Peyratout, A. Smith, J. Sanz, S. Rossignol, Structural characterization of geomaterial foams — thermal behavior, *J. Non-Cryst. Solids* 357 (2011) 3637–3647, <https://doi.org/10.1016/j.jnoncrsol.2011.06.033>.
- [88] K.S.P. Karunadasa, C.H. Manaratne, H. Pitawala, R.M.G. Rajapakse, Thermal decomposition of calcium carbonate (calcite polymorph) as examined by in-situ high-temperature X-ray powder diffraction, *J. Phys. Chem. Solid.* 134 (2019) 21–28.
- [89] E. Nielsen, P. Nørhede, O. Ladefoged, L. Tobiassen, Evaluation of Health Hazards by Exposure to Mineral Wools (Glass, Stone/slag, HT) and Proposal of a Health-Based Quality Criterion for Ambient Air, 2013. <https://www2.mst.dk/Udgiv/publications/2013/12/978-87-93026-68-1.pdf>.
- [90] Z. Li, X. Liang, C. Liu, M. Liang, K. van Breugel, G. Ye, Thermal deformation and stress of alkali-activated slag concrete under semi-adiabatic condition: experiments and simulations, *Cement Concr. Res.* 159 (2022) 106887.
- [91] P.N. Lemougna, J. Yliniemi, H. Nguyen, E. Adesanya, P. Tanskanen, P. Kinnunen, J. Roning, M. Illikainen, Utilisation of glass wool waste and mine tailings in high performance building ceramics, *J. Build. Eng.* 31 (2020) 101383, <https://doi.org/10.1016/j.jobte.2020.101383>.
- [92] Z. Li, Z. Deng, X. Guo, An analysis of the microscopic cracking mechanism of hardened alkali-activated slag, *Construct. Build. Mater.* 170 (2018) 466–484.